



## **Cold-Formed Steel Lipped Channel Beams under Fire Conditions: Distortional Response, Failure and DSM Design**

A. Landesmann<sup>1</sup>, D. Camotim<sup>2</sup>

### **Abstract**

The aim of this paper is to report an ongoing shell finite element investigation on the distortional post-buckling behavior, ultimate strength and design of cold-formed steel single-span lipped channel beams subjected to elevated temperatures caused by fire conditions. The beam ultimate strengths are computed by means of a steady-state loading strategy that consists of applying an increasing major-axis uniform bending moment to a beam under a uniform (elevated) temperature distribution, in order to obtain the corresponding failure moments). The steel constitutive law at elevated temperatures is simulated by means of the stress-strain-temperature models prescribed in EC3-1.2 for cold-formed steel. The materially and geometrically non-linear response of the cold-formed lipped channel beams is determined by means of ANSYS non-linear shell finite element analyses that incorporate critical-mode initial geometrical imperfections. Finally, since there are no specific rules to predict the bending strength of cold-formed steel beams failing distortionally when subjected to elevated temperatures, the above failure moments and temperature values will be used to establish guidelines for the design of cold-formed steel lipped channel beams under fire conditions. The approach followed is based on the increasingly popular Direct Strength Method, already employed by other researchers (*e.g.*, Ranawaka and Mahendran 2009b) – the currently available design/strength equations/curves, developed for ambient temperature, are modified to account for the appropriate Young's modulus and yield stress reductions due to the temperature increase.

### **1 Introduction**

The use of cold-formed steel structures has grown steadily during the last few years, as they became extremely popular in different areas of the construction industry, namely in (i) low rise official, residential and industrial buildings, (ii) high storage structures and (iii) roof trussed structures. Cold-formed steel offers very attractive design solutions that exhibit a high structural efficiency (strength-to-weight ratio) and have been characterized by high fabrication versatility and increasingly low production and erection costs. The knowledge about the structural behavior of cold-formed steel members at room temperature has advanced considerably in the last few years and, moreover, such advances have been incorporated into design specifications at a fairly rapid rate. Since it is well known that many cold-formed steel members are prone to distortional failure, the current design specifications include provisions dealing with this collapse mode. In particular, the Direct Strength Method (DSM – *e.g.*, Schafer 2008), which has already been incorporated into the previous and current versions of the North-American

---

<sup>1</sup> Civil Engineering Program, COPPE, Federal University of Rio de Janeiro, Brazil. <alandes@coc.ufrj.br>

<sup>2</sup> Civil Engineering Department, ICIST, Instituto Superior Técnico, University of Lisbon, Portugal. <dcamotim@civil.ist.utl.pt>

(AISI 2012), Australian/New Zealand (AS/NZS 2005) and Brazilian (ABNT 2010) specifications for cold-formed steel structures, includes specific provisions (strength curves) for the design of columns and beams against distortional failure – their application requires only knowledge about the steel yield stress and member distortional buckling load or moment. However, such provisions/curves were developed for cold-formed steel members at room temperature and it is still unknown whether they can also be adopted (with or without modifications) to estimate the ultimate strength of members subjected to elevated temperatures caused by fire conditions, which may alter considerably the steel constitutive law, namely its Young’s modulus, yield strength and amount of non-linearity.

The high “section factor”<sup>3</sup>, associated with the use of (i) high-strength steels and (ii) very slender cross-sections, is responsible for making cold-formed steel construction significantly vulnerable to fire conditions. Therefore, the application of the currently available design methods requires the extensive use of costly fireproofing materials, aimed at protecting the steel structures from an excessive heat increase due to fire hazards. This requirement leads quite often to overly conservative (*i.e.*, unduly uneconomical) structural designs. Moreover, it is fair to say that the research activity devoted to cold-formed steel members under fire conditions was only initiated in this century and is still rather scarce, as attested by the relatively small number of available publications on the subject. Without claiming to be exhaustive, such publications report essentially the work done by Outinen *et al.* (2000), Kaitila (2002), Feng *et al.* (2003a-d, 2004), Lee *et al.* (2003), Zhao *et al.* (2005), Feng and Wang (2005a,b), Chen and Young (2006, 2007a,b, 2008), Ranawaka (2006), Lim and Young (2007), Ranawaka and Mahendran (2009a,b, 2010), Landesmann and Camotim (2010a,b, 2011, 2012a,b) and Shahbazian and Wang (2011a,b, 2012, 2013, 2014), Kankanamge and Mahendran (2012), Chen *et al.* (2012, 2013), Abreu and Schafer (2013), Gunalan and Mahendran (2013a,b), Gunalan *et al.* (2013), Ellobody (2013) and Laím *et al.* (2014). Moreover, only a small fraction of these studies addresses failures associated with the occurrence of distortional buckling, an instability phenomenon often governing the behavior and strength of lipped members with intermediate unrestrained lengths. Moreover, although a considerable amount of research has been conducted on the distortional behavior of cold-formed steel beams (*e.g.*, Yu and Schafer 2007, Dinis and Camotim 2010, Haidarali and Nethercot 2012, Kalkan and Buyukkaragoz 2012 or Andreassen and Jönsson 2013) to the authors’ best knowledge no research activity has been reported on such behavior at elevated temperatures. Therefore, the objective of this paper is to provide a contribution towards filling this gap, by presenting and discussing the available results of an ongoing shell finite element investigation on the distortional post-buckling behavior, ultimate strength and design of cold-formed steel single-span lipped channel beams subjected to elevated temperatures due to fire conditions.

The paper begins by presenting the beam geometry selection, achieved by means of sequences of “trial-and-error” buckling analyses (Section 2). It aims at identifying beam cross-section dimensions and lengths leading to, as much as possible, “pure” distortional buckling and failure modes – *i.e.*, the selected beams exhibit distortional critical buckling moments that are significantly lower than their local and global counterparts. Then, Section 3 briefly describes the shell finite element model employed to perform the geometrically and materially non-linear analyses in the commercial code ANSYS (SAS 2009) for room and elevated temperatures. Section 4 is devoted to room temperature analysis and starts with the validation of the ANSYS shell finite element model employed, through the reproduction of available numerical simulations (Yu and Schafer 2007). Next, illustrative numerical results concerning the beam distortional

---

<sup>3</sup> The heating rate of a given cross-section varies according to its dimensions, namely the so-called “section factor”, which is given by the  $H_p/A$  relationship, where (i)  $H_p$  is the steel cross-section perimeter exposed to the fire and (ii)  $A$  is the cross-sectional area. A larger  $H_p/A$  value corresponds to a higher susceptibility to fire effects (or, alternatively, to a higher need for using fireproofing materials).

post-buckling behavior and ultimate strength are presented and discussed. Moreover, the trends of the numerical ultimate strength data are compared with experimental and numerical values reported in the literature, and a comparison between the numerical and experimental ultimate moment values and their estimates provided by the current DSM design curve/expressions are presented and discussed, making it possible to obtain a preliminary assessment of how the “quality” of the latter is influenced by the beam geometry and (mostly) end support conditions. Finally, Section 5 addresses the influence of the temperature (according to the EC3-1.2 temperature-dependent steel constitutive law) on the pin-ended beam elastic-plastic post-buckling and ultimate strength behaviors and corresponding DSM design.

## 2 Beam Geometry Selection – Buckling Behavior

The first task in this work consisted of carefully selecting the cross-section dimensions and lengths of the cold-formed steel single-span lipped channel beams to be analyzed, which exhibit two different end support conditions: “fixed” (F) and “pinned” (P). These designations concern the warping displacements and local rotations, which may be prevented (F) or free (P) – in both cases, the global major/minor-axis rotations are free and the torsional rotations are prevented. The selection procedure involved sequences of “trial-and-error” buckling analyses, performed by means of either (i) analyses based on Generalized Beam Theory (GBT – code GBTUL, developed by Bebiano *et al.* 2008a,b) or (ii) ANSYS shell finite element analyses (SFEA), aimed at satisfying the following requirements:

- (i) Beams buckling in “pure” distortional modes and also exhibiting distortional collapses. This goal is achieved by ensuring that the critical buckling moment ( $i_1$ ) is clearly distortional and ( $i_2$ ) falls considerably below the lowest local and global bifurcation moments.
- (ii) Cross-section (lipped channel) dimensions associated with “pure” distortional failures for both end support conditions dealt with here (only the lengths are different). Although this requirement is by no means essential, it makes the performance of the parametric study obviously easier.
- (iii) Beam lengths ( $iii_1$ ) associated with single half-wave buckling modes and ( $iii_2$ ) as close as possible to the values of the P-beam minimum distortional critical buckling moments.
- (iv) Cross-section dimensions commonly used in practice and, if possible, distinct wall width proportions, namely web-to-flange width ratios. This requirement is intended to enable assessing whether such width proportions have a meaningful influence on the beam distortional post-critical strength.

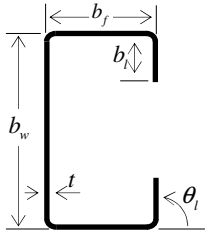
Fortunately, it was possible to fulfill all the above requirements and the end product of the “trial-and-error” selection procedure are the 3 cross-section dimensions given in Table 1 – their web-to-flange width ratio are equal 1.25 and 1.6 (twice)<sup>4</sup>. On the other hand, Table 2 provides, for each beam geometry, (i) the length associated with critical distortional buckling ( $L_D$ ), (ii) the corresponding critical (distortional) buckling moment at room temperature ( $M_{cr,D,20}$ ) and (iii) its ratios with respect to the lowest local ( $M_{bl,L,T}$ ) and global ( $M_{bl,e,T}$ ) bifurcation moments – all the buckling/bifurcation moments were calculated for  $E_{20}=210\text{ GPa}$  (steel Young’s modulus at room temperature) and  $\nu=0.3$  (Poisson’s ratio, assumed not to vary with the temperature). One observes that the first “non-distortional” buckling moment always corresponds to local buckling and that the ratio  $M_{bl,L,T}/M_{cr,D,T}$  varies between 2.63 and 3.72 (P-beams) and 1.83 and 2.57 (F-beams). The first global (lateral-torsional) buckling moment is invariably much higher – indeed, the  $M_{bl,e,T}/M_{cr,D,T}$  ratio values vary from 39.4 to 105.7 (P-beams) and from 25.28 to 93.03 (F-beams).

---

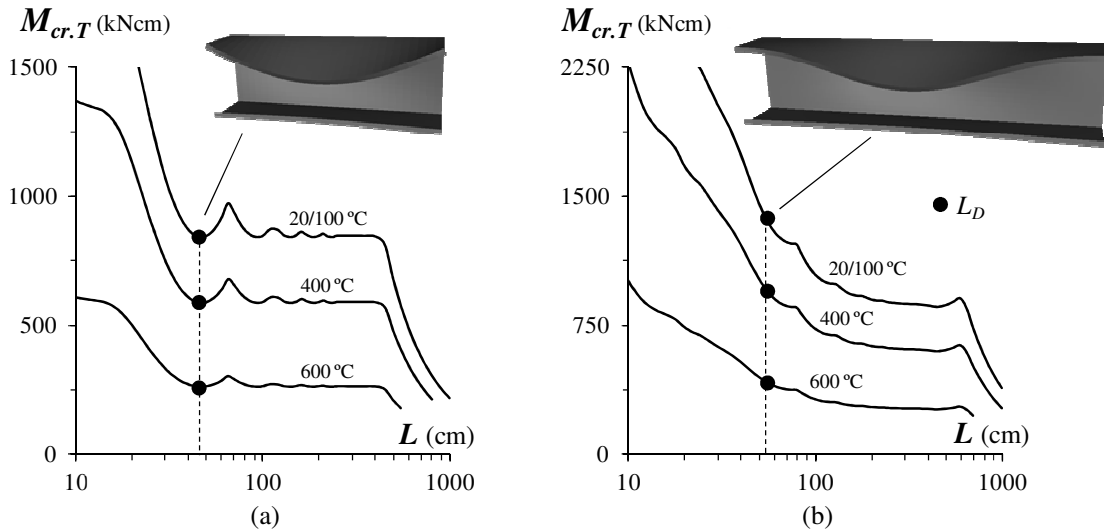
<sup>4</sup> It was found that fulfilling the requirement of obtaining a wide range of web-to-flange width ratios is not such and easy task.

**Table 1.** Cross-section dimensions and area of selected C-lipped beams

Cross-section	$b_w$ (mm)	$b_f$ (mm)	$b_l$ (mm)	$t$ (mm)	$\theta_l$ (deg)	Area (cm <sup>2</sup> )
C120	120	75	10	3	90	8.7
C150	150	120	10	3.5	90	14.4
C160	160	100	10	2.2	90	8.4


**Table 2.** Selected lipped channel beam lengths, critical buckling moments and bifurcation-to-critical moment ratios

Beam	Pinned (P)				Fixed (F)			
	$L_D$ (cm)	$M_{cr,D,20}$ (kNcm)	$\frac{M_{bl,L,T}}{M_{cr,D,T}}$	$\frac{M_{bl,e,T}}{M_{cr,D,T}}$	$L_D$ (cm)	$M_{cr,D,20}$ (kNcm)	$\frac{M_{bl,L,T}}{M_{cr,D,T}}$	$\frac{M_{bl,e,T}}{M_{cr,D,T}}$
C120	32	1788.1	3.29	39.34	50	2580.6	2.33	25.28
C150	42	1904.9	3.72	105.68	55	2857.7	2.57	93.03
C160	46	841.8	2.63	86.19	70	1236.5	1.83	57.42

**Figure 1.** Variation of  $M_{cr,T}$  with  $L$  and  $T$  for (a) P and (b) F C120 beams (EC3-1.2 model)

The curves depicted in Figs. 1(a)-(b) provide the variation of  $M_{cr,T}$  (elastic critical buckling moments for different temperatures) with the length  $L$  (logarithmic scale) and temperature  $T$  for P and F beams with the C120 cross-section dimensions. Note that (i) three temperatures are dealt with ( $20/100^\circ\text{C}$ , *i.e.* room temperature,  $400^\circ\text{C}$  and  $600^\circ\text{C}$ ), (ii) the vertical scales are different in Figs. 1(a) and 1(b) and (iii) the EC3-1.2 (2005) constitutive model, presented in some detail in Section 3, is adopted. Also shown are the critical (distortional) buckling mode shapes of the P-beam with  $L_D=32\text{ cm}$  and F-beam with  $L_D=50\text{ cm}$ . Note that any given buckling curve can be obtained through a “vertical translation” of the top one, with a magnitude that depends exclusively on the Young’s modulus erosion due to the temperature rise<sup>5</sup>. Moreover, the critical distortional moment  $M_{cr,D,T}$  corresponds to the same length ( $L_D$ ) for each temperature value.

<sup>5</sup> Naturally, the Young’s modulus reduction factor  $k_e$ , whose variation with the temperature  $T$  is illustrated in Fig. 2(a), makes it possible to quantify the decrease in the beam critical buckling moment  $M_{cr,T}$  associated with a given length.

### 3 Numerical Model

The beam distortional post-buckling equilibrium paths and ultimate strength values were determined through ANSYS (2009) geometrically and materially non-linear SFEA. The beams were discretized into SHELL181 elements (ANSYS nomenclature – 4-node shear deformable thin-shell elements with six degrees of freedom per node and full integration). The analyses (i) were performed by means of an incremental-iterative technique combining Newton-Raphson’s method with an arc-length control strategy and (ii) simulate the response of beams subjected to uniform/constant temperature distributions (*i.e.*, the beams are deemed engulfed in flames, thus sharing the surrounding air temperature – Landesmann *et al.* 2009) and subsequently acted by an increasing uniform major-axis bending moment up until failure – steady state structural analyses providing failure moments<sup>6</sup>.

As stated earlier, the simply supported beams analyzed exhibit two end support conditions, differing in the warping displacements and local displacements/rotations, which can be either free (P-beams) or prevented (F-beams) – the latter are modeled by attaching rigid plates to the beam end cross-sections. The uniform bending moment diagram is achieved through the application of either (i) sets of concentrated forces acting on the nodes of both end cross-sections section (P-beams) or (ii) two concentrated moments acting on the rigid end-plates (F-beams). The force/moment application is made in small increments, taking advantage of the ANSYS automatic “load stepping procedure”.

All the beams contained initial geometrical imperfections with a critical-mode (distortional) shape and small amplitude (10% of the wall thickness  $t$ ). These initial imperfections involve inward compressed flange-lip motions, since they are most detrimental, in the sense of leading to lower post-buckling strengths (Dinis and Camotim 2010). Each critical buckling mode shape was determined by means of a preliminary ANSYS buckling analysis, performed with exactly the same shell finite element mesh employed to carry out the subsequent non-linear (post-buckling) analysis – this procedure makes it very easy to “transform” the buckling analysis output into a non-linear analysis input. It is still worth noting that no strain-hardening, residual stresses and/or corner strength effects were considered in this work.

#### 3.1 Steel Material Behavior

The multi-linear stress-strain curve available in ANSYS code is adopted to model the steel material behavior for several yield stresses<sup>7</sup>. The steel constitutive law at elevated temperatures adopted to carry out the research work reported in this paper is defined by the analytical expression provided in Part 1.2 of Eurocode 3 (EC3-1.2 2005). Fig. 2(a) makes it possible to compare the temperature variations of the cold-formed steel reduction factors applicable to the steel Young’s modulus ( $k_e = E_T/E_{20}$ ) nominal yield stress ( $k_y = \sigma_{y,T}/\sigma_{y,20}$ ) and proportionality limit stress ( $k_p = \sigma_{p,T}/\sigma_{p,20}$ ), which are tabulated in EC3-1.2. As for Fig. 2(b), it illustrates the qualitative differences between the steel stress-strain curves prescribed by the EC3-1.2 model for  $T=20/100$  °C (room temperature),  $T=400$  °C,  $T=600$  °C and  $T=800$  °C –  $\sigma_T/\sigma_{y,20}$  vs.  $\epsilon$ , where the applied stress at a given temperature,  $\sigma_T$ , is normalized with respect to the room temperature yield stress  $\sigma_{y,20}$ . Note that the steel stress-strain curve non-linearity increases substantially with the temperature (for  $T=20/100$  °C, the EC3-1.2 model prescribes a bi-linear constitutive law, corresponding to an elastic-perfectly plastic material). The corresponding stress-strain curve, given by

---

<sup>6</sup> Not that the authors (Landesmann & Camotim 2010a,b) showed that the failure loads yielded by the steady state analyses match the more realistic failure temperatures obtained through the “corresponding” transient analyses (axially compressed columns heated up to failure).

<sup>7</sup> Note that a considerable large fraction of the yield stresses considered in this work are unrealistically high, leading to  $E_{20}/\sigma_{y,20}$  values that largely exceed the current DSM limit for pre-qualified beams ( $E_{20}/\sigma_{y,20}=340$ ). The reason for selecting such high yield stresses was to enable the analysis slender and very slender beams, *i.e.*, to make it possible to cover a wide beam slenderness range.

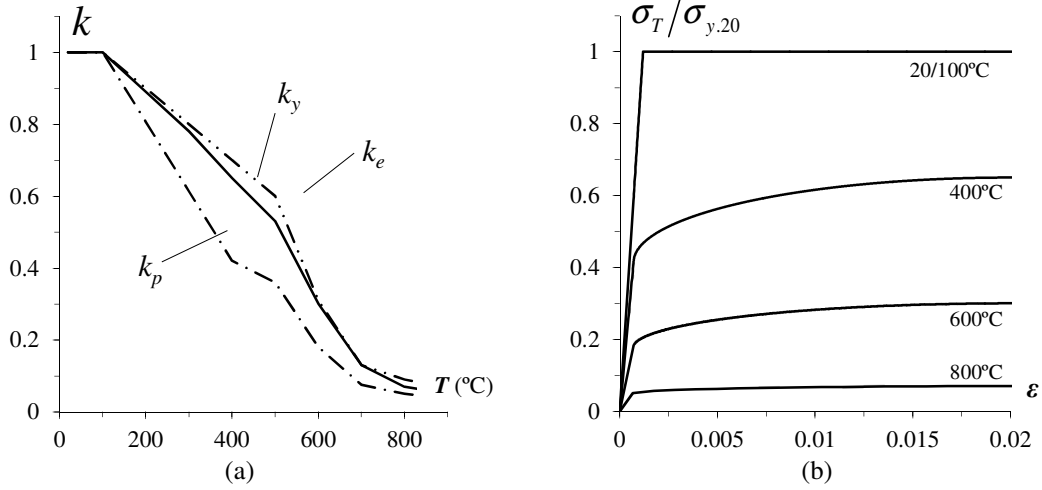


**Figure 2.** (a) Variation of the reduction factors  $k_e$ ,  $k_y$ ,  $k_p$  with  $T \leq 800^\circ\text{C}$  and (b) cold-formed steel stress-strain curves  $\sigma_T/\sigma_{y,20}$  vs.  $\varepsilon$  ( $\varepsilon \leq 2\%$ ) for  $T=20/100-400-600-800^\circ\text{C}$  – EC3-1.2 model

$$\sigma_T = \begin{cases} \varepsilon \cdot E_T & \text{for } \varepsilon \leq \varepsilon_{p,T} \\ \sigma_{p,T} - c + (b/a) \left[ a^2 - (\varepsilon_{y,T} - \varepsilon)^2 \right]^{0.5} & \text{for } \varepsilon_{p,T} < \varepsilon < \varepsilon_{y,T} \\ \sigma_{y,T} & \text{for } \varepsilon_{y,T} \leq \varepsilon \leq \varepsilon_{u,T} \end{cases}, \quad (1)$$

$$a^2 = (\varepsilon_{y,T} - \varepsilon_{p,T})(\varepsilon_{y,T} - \varepsilon_{p,T} + c/E_T), \quad b^2 = c(\varepsilon_{y,T} - \varepsilon_{p,T})E_T + c^2,$$

$$c = \frac{(\sigma_{y,T} - \sigma_{p,T})^2}{(\varepsilon_{y,T} - \varepsilon_{p,T})E_T - 2(\sigma_{y,T} - \sigma_{p,T})}$$

is divided into three regions, associated with distinct strain ranges<sup>8</sup>. Notice that the stress-strain curve shape is considerably influenced by the temperature and proportionality limit strain ( $\varepsilon_{p,T} = \sigma_{p,T}/E_T$ ). The first part of the well-defined yield plateau exhibited by the  $T=20/100^\circ\text{C}$  curve is replaced by a strain-hardening region that becomes more pronounced as the temperature rises. The stress-strain curve (i) is linear elastic, with slope  $E_T$  ( $E_{20}=210\text{ GPa}$ ), up to the proportional limit  $\sigma_{p,T}$ , then (ii) becomes elliptic in the region associated with the transition between the elastic and plastic ranges, up to the effective yield stress  $\sigma_{y,T}$  (corresponding to  $\varepsilon_{y,T}=0.02$ ), which accounts for (kinematic) strain-hardening and (iii) ends with a perfectly flat yield plateau up to a limit strain  $\varepsilon_{u,T}=0.15$  – in all cases, Prandtl-Reuss's plasticity model (von Mises yield criterion and associated flow rule) is adopted. Finally, since the distortional post-buckling analyses carried out involve large inelastic strains, the nominal (engineering) static stress-strain curve is replaced by a relation between the true stress and the logarithmic plastic strain.

#### 4 Distortional Response at Room Temperature

Besides the validation of the above ANSYS SFE model, this section includes also the presentation and discussion of numerical model results concerning the influence of the cross-section dimensions and end support conditions on the beam distortional post-buckling behavior and strength. Elastic and elastic-plastic numerical results are addressed separately.

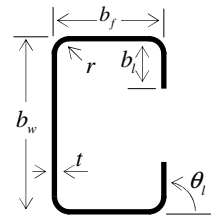
<sup>8</sup> Although the EC3-1.2 model further extends the stress-strain relationship, to include strain-hardening, for steel temperatures below  $400^\circ\text{C}$  (this strain-hardening is negligible for temperatures higher than  $400^\circ\text{C}$ ), this effect is not considered in the present work.

#### 4.1 Validation Studies

In order to validate the use of the ANSYS shell finite element model to assess the distortional post-buckling behavior and strength of cold-formed steel beams, one begins by reproducing numerical simulations reported by Yu and Schafer (2007), concerning cold-formed steel lipped channel beams that originated from experimental tests carried out by these authors. The cross-section dimensions considered here are given in Table 3 and consist of mean values of the dimensions/angles adopted by Yu and Schafer (2007) in their extensive numerical analyses (including many beams that were not experimentally tested).

**Table 3.** Beam cross-section dimensions selected from the extended finite element analyses of Yu and Schafer (2007)

Cross-section	$b_w$ (mm)	$b_f$ (mm)	$b_l$ (mm)	$t$ (mm)	$r$ (mm)	$\theta_l$ (deg)
8C097	204.216	52.832	14.097	2.4892	7.11	85.7



It is important to realize that the numerical analyses performed by Yu and Schafer (2007) were aimed at simulating the experimental tests carried out by these authors: four-point bending tests of beams formed by assemblages of two identical lipped channel members (i) with an overall length of  $487.68\text{ cm}$  ( $16\text{ ft}$ ), (ii) acted by two in-span point loads applied at the  $1/3$  points and (iii) connected together back-to-back (to avoid applied torsion) by means of (rigid) hot-rolled tubes bolted to both webs and located at the end and loaded cross-sections (avoiding also shear and web crippling problems). While the beam central  $1/3$ -span (with length  $162.56\text{ cm}$  and subjected to uniform bending) was basically unrestrained<sup>9</sup>, a through-fastened steel decking was attached (screwed) to stabilize the compression flange along the two outer spans – Fig. 3(a), taken from Yu and Schafer (2007), provides an overall view of the experimental test set-up.

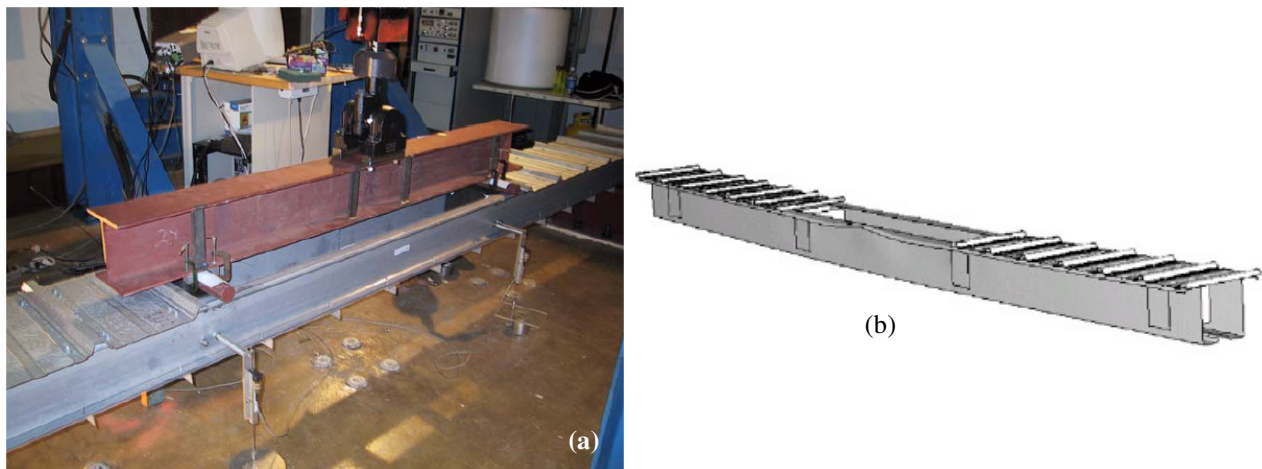


**Figure 3.** (a) Experimental test set-up and (b) corresponding finite element model used by Yu and Schafer (2007).

Since Yu and Schafer wanted to simulate the performance of the real tests, they modeled the whole experimental set-up, including the cold-formed steel beams, steel decking and hot-rolled tubes. The software used was ABAQUS and the 8C097 beam itself was discretized by means of  $25.4\text{ mm} \times 25.4\text{ mm}$  meshes of S4R shell finite elements (ABAQUS nomenclature – 4-node isoparametric thin-shell elements

<sup>9</sup> In view of this experimental set-up, the two lipped channels “work almost independently” in the beam central span – indeed, the word “almost” stems from the fact that small angles ( $1\frac{1}{4} \times 1\frac{1}{4} \times 0.057\text{ in}$ ) were attached (screwed) to the tension flanges every  $12\text{ in}$  (see Fig. 3(a)).

with six degrees of freedom per node and reduced shear integration). As for the steel material properties adopted in the numerical simulations, they were the following:  $E=203.4 \text{ GPa}$  ( $29500 \text{ ksi}$ ),  $\nu=0.3$  and  $\sigma_{y,20}=227.53\text{-}303.37\text{-}386.80\text{-}428.85\text{-}506.08 \text{ MPa}$  ( $33\text{-}44\text{-}56.1\text{-}62.2\text{-}73.4 \text{ ksi}$ ). Finally, the beams were analyzed with critical-mode (distortional) initial geometrical imperfections with amplitude equal to  $0.94t$  (residual stresses and corner strength enhancement effects were neglected). An overall view of the finite element model used by Yu and Schafer to simulate their experimental test set-up is shown in Fig. 3(b).

On the other hand, the numerical analyses carried out in this work were performed in the code ANSYS and adopting the models described in section 3 – the underlying structural models are obviously much simpler, mainly because the end support conditions are very well defined (in clear contrast with those adopted by Yu and Schafer, who aimed at simulating, as realistically as possible, a rather complex experimental set-up). Indeed, the model adopted in this work merely consists of a single-span simply supported lipped channel beam (not beam pair) (i) with length  $L=162.56 \text{ cm}$  (like the central span of the three-span beam of Yu and Schafer) and the cross-section dimensions given in Table 3, (ii) exhibiting an elastic-perfectly plastic material behavior with five yield stresses (also considered by Yu and Schafer – see Table 4), (iii) acted by equal end moments and (iii) containing critical-mode (distortional) initial geometrical imperfections with amplitude equal to 94% of the wall thickness (like the beam of Yu and Schafer). Concerning the end support conditions, an F-beam (see section 3) is analyzed and, in order to replicate more closely the experimental set-up of Yu and Schafer, the minor-axis flexural rotations are prevented – *i.e.*, as far as the global flexural deformations are concerned, the beam is simply supported for major-axis bending and fixed for minor-axis bending. Moreover, the rounded corners were included in the cross-section model (radius given in Table 3)<sup>10</sup>. The ultimate moments obtained in this work ( $M_{u,obt}$ ) are compared with those reported by Yu and Schafer (2007)<sup>11</sup> ( $M_{u,YS}$ ) in Table 4 for beams with the five yield stresses  $\sigma_{y,20}=227.53\text{-}303.37\text{-}386.80\text{-}428.85\text{-}506.08 \text{ MPa}$  – Figs. 4(a)-(b) show the distortional critical buckling mode and failure mode shapes of the beam with  $\sigma_{y,20}=386.80 \text{ MPa}$ . The percentage differences between the  $M_{u,obt}$  and  $M_{u,YS}$  values, also given in Table 4, never exceed 4.4% and, with a single exception, the values obtained here are higher, probably because the model of Yu and Schafer does not ensure fully warping and minor-axis flexural fixity. This assertion is confirmed by the difference between the critical (distortional) buckling moments of the beam with  $\sigma_{y,20}=386.80 \text{ MPa}$ :  $3022.90 \text{ kNcm}$  vs.  $2915.01 \text{ kNcm}$ , which corresponds to a 3.7% difference. In view of the above comparison, it seems fair argue that the shell finite element model employed in this work may be deemed as validated.

**Table 4.** Beam ultimate bending moment reported by Yu and Schafer ( $M_{u,YS}$ ) and obtained ( $M_{u,obt}$ )

$\sigma_{y,20}$ (MPa)	$M_{u,YS}$ (kN·cm)	$M_{u,obt}$ (kN·cm)	$\frac{M_{u,YS} - M_{u,obt}}{M_{u,YS}}$
227.53	1042.85	1010.60	3.1%
303.37	1333.22	1274.20	4.4%
386.80	1588.57	1527.00	3.9%
428.85	1675.57	1645.10	1.8%
506.08	1839.39	1849.35	-0.5%

<sup>10</sup> The inclusion of the rounded corner is restricted to this validation study – in all the remaining numerical results presented and discussed in this work, both at room and elevated temperatures, this effect is ignored and sharp corners are considered.

<sup>11</sup> These results are given for a beam with a single lipped channel cross-section, *i.e.*, Yu and Schafer (2007) halved the numerical values obtained from their analyses, which involved beams with cross-sections consisting of two identical lipped channels.



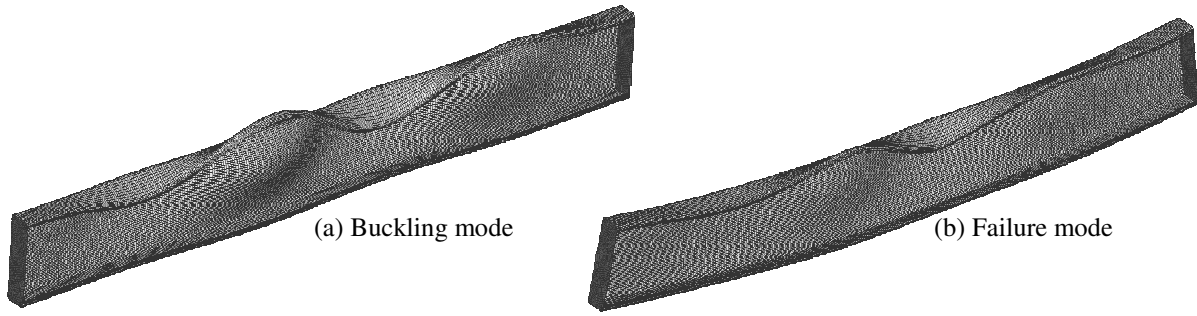


**Figure 4.** 8C097 beam distortional (a) critical buckling mode and (b) failure mode shapes ( $\sigma_{y,20} = 386.80 \text{ MPa}$ )

#### 4.2 Elastic Post-Buckling Behavior

Figs. 5(a)-(b) show the elastic post-buckling equilibrium paths obtained for the P and F C120-150-160 beams, relating the applied bending moment  $M$ , normalized *w.r.t.*  $M_{cr,D,20}$ , to the normalized displacement  $|\delta|/t$ , where  $|\delta|$  is the mid-span (maximum) vertical displacement of the compressed flange-stiffener corner and  $t$  is the wall thickness. The observation of these two sets of distortional post-buckling equilibrium paths prompts the following remarks:

- (i) First of all, the higher stiffness and strength of the F-beams is amply confirmed by comparing Figs. 5(a) and 4(b). Moreover, there is also a clear difference between the P-beam and F-beam equilibrium path shapes: while the former exhibit a pronounced convexity, which is associated with progressive stiffness degradation that leads to elastic limit points (visible in the C120-160 beams), the latter display a concavity, which stems from the stiffness increase provided by the warping fixity of the end supports and precludes the occurrence of an elastic limit point (at least for an acceptable, *i.e.*, not too high displacement value).
- (ii) Regarding the influence of the cross-section dimensions, one immediately notices the similarity between C120 and C160 beam stiffness and strength values – note that they share exactly the same  $b_w/b_f = 1.60$  value). For the F-beams, they are virtually identical for the whole displacement range displayed. For the P-beams, on the other hand, the equilibrium paths coincide up to  $|\delta|/t \approx 9$ , when the C120 beam equilibrium path quickly evolves towards its limit point – conversely, the C160

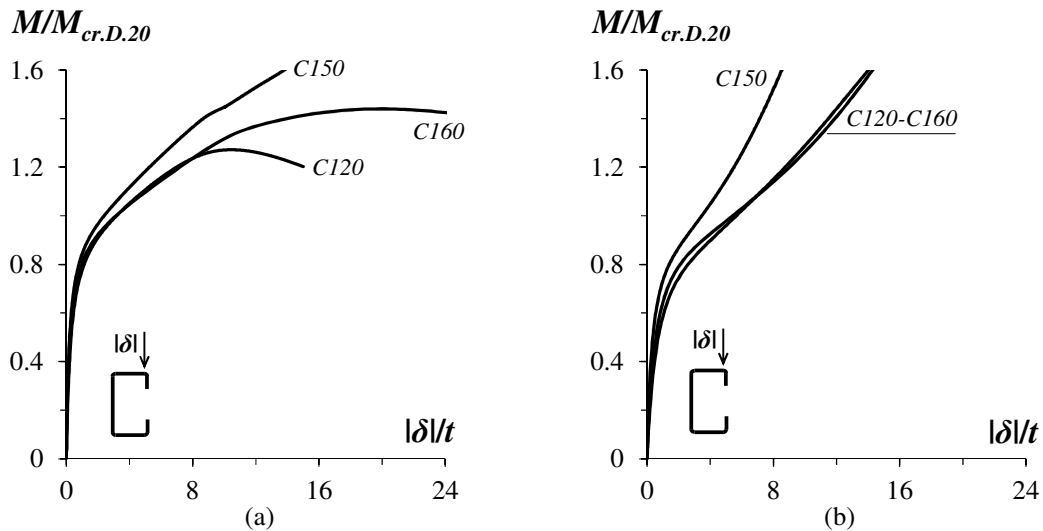


**Figure 5.** Elastic equilibrium paths  $M/M_{cr,D,20}$  vs.  $|\delta|/t$  concerning the (a) P and (b) F C120-150-160 beams

beam equilibrium path exhibits much more ductility prior to failure. Although no sound mechanical reason was (yet) found for this behavioral difference, it should be noticed that the C120 beam is thicker (3.0 mm vs. 2.2 mm) and has “more effective” lips (higher  $b_l/b_f$  value: 0.133 vs. 0.100).

- (iii) Both the P and F C150 beams have clearly higher post-critical stiffness and strength values than their C120 and C160 counterparts. This is most certainly a consequence of its lower  $b_w/b_f=1.25$  value and higher thickness, which implies that the elastic rotational restraint provided by the web to the compressed flange-lip assembly is significantly higher.
- (iv) In spite of its extremely limited scope (only 6 beams analyzed), this study makes it possible to anticipate that both the end support conditions and the cross-section dimensions are bound to affect considerably the characteristics of the beam elastic distortional post-buckling stiffness and strength, which may have non-negligible implications on the corresponding (elastic-plastic) ultimate strength and, therefore, also on its prediction by design methods. This issue deserves further investigation in the future<sup>12</sup>.

### 4.3 Elastic-Plastic Post-Buckling Behavior and Strength

The ANSYS shell finite element model validated in the previous section is now employed to perform a parametric study aimed at assessing the elastic-plastic post-buckling and ultimate strength behaviors of P and F beams buckling and failing in distortional modes. The numerical results presented and discussed concern a total of 110 beams, corresponding to a combination of (i) the 3 beams geometries defined in Tables 1 and 2, (ii) the 2 end support conditions dealt with in this work (P and F) and (iii) several room temperature yield stresses<sup>13</sup>, selected to enable covering wide distortional slenderness ranges for all beam sets:  $\lambda_{D,20}$  varies from 0.46 to 3.37 (P-beams) and from 0.38 to 2.94 (F-beams) – recall that  $\lambda_{D,20}=[M_{y,20}/M_{cr,D,20}]^{0.5}$ , where  $M_{y,20}=S\cdot\sigma_{y,20}$  and  $S$  is the major-axis elastic section modulus. Tables A1 to A3, included in Annex A, provide, for each beam analyzed, the (i) yield stress  $\sigma_{y,20}$ , (ii) yield moment  $M_{y,20}$ , (iii) distortional slenderness  $\lambda_{D,20}$ , (iv) ultimate moments  $M_{u,20}$  and corresponding limit point  $|\delta|/t$  value, denoted  $(|\delta|/t)_{lim}$ , and (v) ultimate moment ratios  $M_{u,20}/M_{cr,D,20}$  and  $M_{u,20}/M_{y,20}$ .

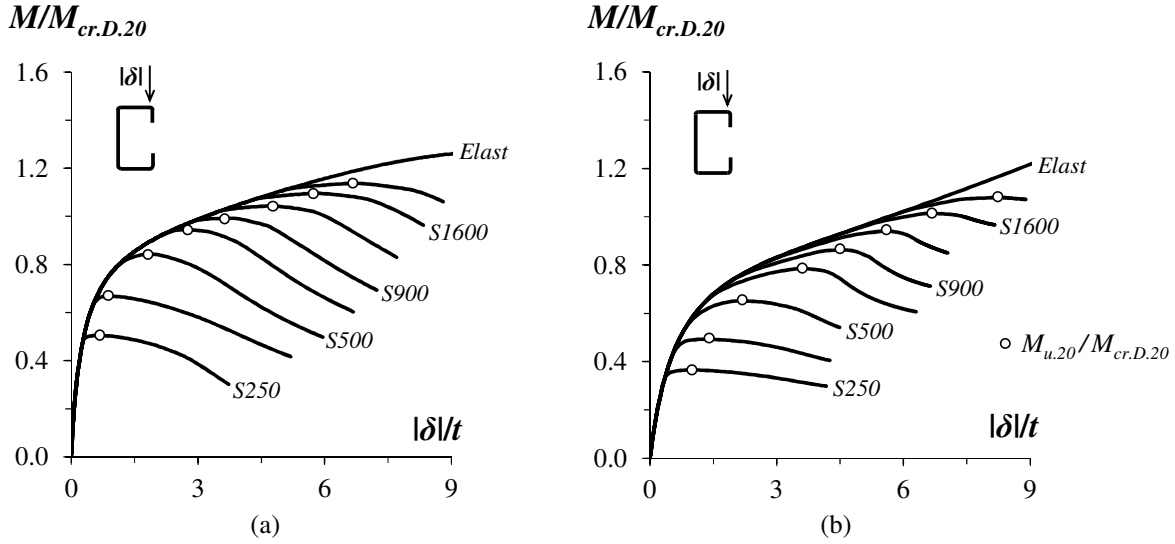
Figs. 6(a)-(b) display, for the two support conditions, a sample of the non-linear (geometrically and materially) equilibrium paths  $M/M_{cr,D,20}$  vs.  $|\delta|/t$  determined to obtain the ultimate moments  $M_{u,20}$  (identified by white circles) – these equilibrium paths concern C120 beams with room temperature yield stresses  $\sigma_{y,20}=250-350-500-700-900-1200-1600-2000\text{ MPa}$ . The elastic equilibrium paths, already shown in Figs. 4(a)-(b), are presented again for comparison purposes<sup>14</sup>. As for Figs. 6(a)-(c), they depict the P and F beam and mid-span cross-section deformed configurations, in the close vicinity of failure, for  $\sigma_{y,20}=250\text{ MPa}$  – the beam collapse distortional nature is clearly shown.

The observation of the results shown in the above figures, as well as the data provided in tables A1 to A3 (see Annex A), leads to the following conclusions:

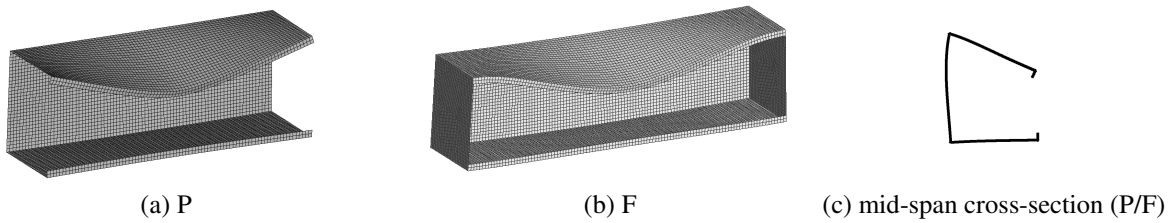
<sup>12</sup> The authors are not aware of any available work on the influence of the cross-section geometry and/or end support conditions in the beam distortional post-buckling behavior. Such an investigation is currently under way in the context of cold-formed steel columns (Landesmann *et al.* 2013).

<sup>13</sup> The following room temperature yield stresses  $\sigma_{y,20}$  were considered: (i) 100-150-200-250-350-500-700-900-1200-1600-2000-2500-3000-3500-4000-4500 MPa (C120 P-beams) and 100-140-180-220-250-350-500-700-900-1200-1600-2000-2500-3000-3500-4000-4500-5000-5500-6000 MPa (C120 F-beams), (ii) 100-140-180-220-250-300-350-400-425-450-475-500-700-900-1200-1600-2000-2500-3000 MPa (C150 P-beams) and, 100-140-180-220-250-300-350-400-425-450-475-500-700-900-1200-1600-2000-2500-3000-3500 MPa (C150 F-beams), and (iii) 50-75-100-140-180-200-220-250-350-500-700-900-1200-1600-2000 MPa (C160 P-beams) and, 40-80-100-140-180-200-220-250-300-350-400-425-450-475-500-700-900-1200-1600-2000 MPa (C160 F-beams).

<sup>14</sup> Note that Figs. 5(a)-(b) only extend up to  $|\delta|/t=9$ , while Figs. 4(a)-(b) extended up to  $|\delta|/t=24$ . This is why the P and F beam equilibrium appear to be much more similar in the former than in the latter.

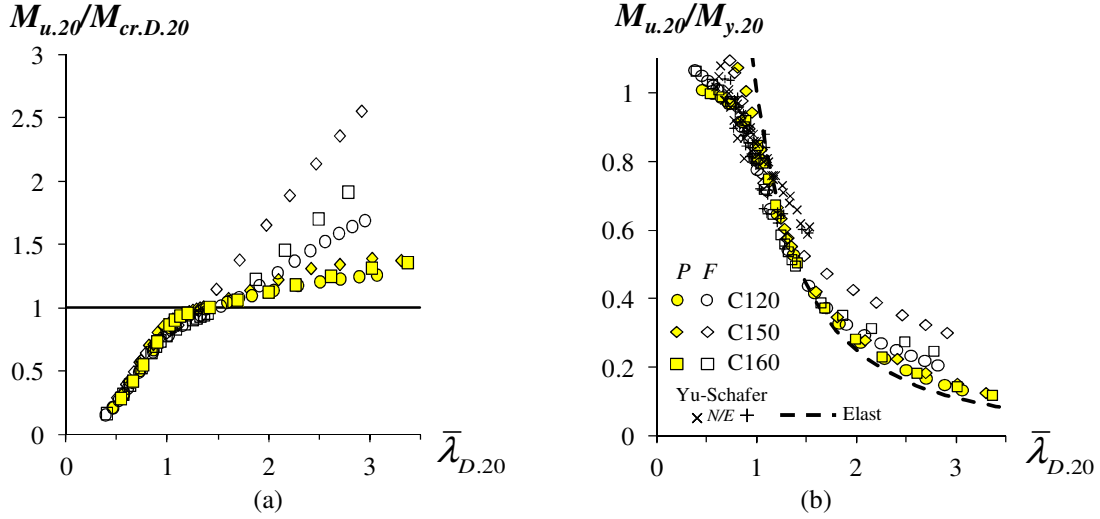


**Figure 6.** Room temperature elastic-plastic distortional equilibrium paths ( $M/M_{cr,D.20}$  vs.  $|\delta|/t$ ) concerning the (a) P and (b) F C120 beams with  $\sigma_{y,20}=250-350-500-700-900-1200-1600-2000\text{ MPa}$



**Figure 7.** Distortional failure modes of the C120 beam with the two support conditions ( $\sigma_{y,20}=250\text{ MPa}$ )

- (i) The P-beam elastic-plastic post-buckling behavior and ultimate strength are different from their F-beam counterparts, both qualitatively and quantitatively— in order to quantify this statement, note that the C120 beam  $M_{u,20}/M_{cr,D.20}$  values are equal to 0.25 and 0.15 ( $\sigma_{y,20}=100\text{ MPa}$ ), 1.10 and 1.01 ( $\sigma_{y,20}=1600\text{ MPa}$ ) and, 1.26 and 1.52 ( $\sigma_{y,20}=4500\text{ MPa}$ ) – note that the F-beam values only exceed their P-beam counterparts for very high yield stress (slenderness) values.
- (ii) The ultimate bending moment ratios  $M_{u,20}/M_{cr,D.20}$  and associated  $(|\delta|/t)_{lim}$  values increase with the yield stresses  $\sigma_{y,20}$ , regardless of the end support condition and cross-section dimensions. Fig. 8(a) plots the  $M_{u,20}/M_{cr,D.20}$  vs.  $\bar{\lambda}_{D,20}$  curves for the P and F beams. It is observed all beam failing below the critical bending moment level (i.e.,  $M_{u,20}/M_{cr,D.20} \leq 1$ ) exhibit a rather small elastic-plastic strength reserve and very little ductility prior to failure – moreover, there are no visible qualitative differences between the values concerning the P and F beams. This assertion does not remain valid when  $M_{u,20}/M_{cr,D.20} > 1$ : while the P-beams collapse almost immediately after the onset of yielding, the F-beams exhibit a considerably higher elastic-plastic strength reserve, which is direct consequence of the elastic post-buckling differences addressed earlier – indeed, one notices that largest post-critical strength reserve is exhibited by the C150 F-beams. Now, differences between the values concerning the P and F beams are very clear (the latter are consistently higher and the differences increase with  $\bar{\lambda}_{D,20}$ ).
- (iii) Both the P and F beams exhibit single half-wave distortional buckling and failure modes – in both cases, failure involves inward displacement of the mid-span compressed flange (see Fig. 7(c)).



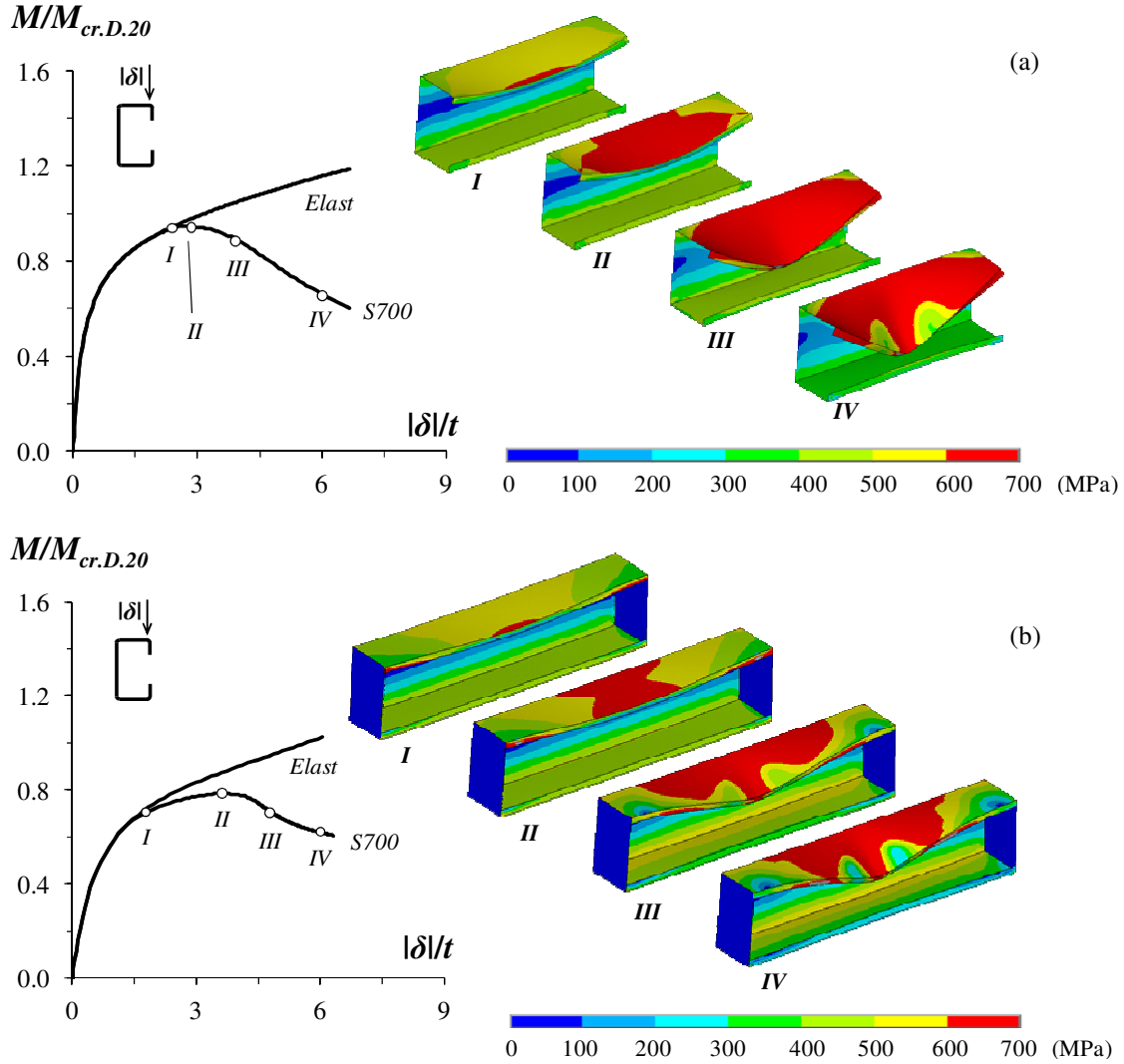
**Figure 8.** Plots of the ultimate bending moment ratios (a)  $M_{u,20}/M_{cr,D,20}$  and (b)  $M_{u,20}/M_{y,20}$  (obtained in this work and reported by Yu and Schafer 2007) against the distortional slenderness  $\bar{\lambda}_{D,20}$

Fig. 8(b) plots the ultimate bending moment ratios  $M_{u,20}/M_{y,20}$  against the distortional slenderness  $\bar{\lambda}_{D,20}$  for the *I10* beams considered in this work and also those numerically analyzed by Yu and Schafer (2007). The observation of this plot shows that:

- (i) As it would be logical to expect, the  $M_{u,20}/M_{y,20}$  vs.  $\bar{\lambda}_{D,20}$  “cloud” follows the trend of a “Winter-type” strength/design curves, without some “vertical dispersion” for all the F-beams (it is minute in the P-beams), due to the differences in elastic-plastic strength reserve – for instance, the C150 F-beam  $M_{u,20}/M_{y,20}$  values are considerably above all the other ones.
- (ii) All the slender P-beams values are fairly well aligned (with very little vertical dispersion) along the elastic buckling strength curve  $1/(\bar{\lambda}_{D,20})^2$  (dashed curve).
- (iii) The numerical results reported by Yu and Schafer (2007), which (iii<sub>1</sub>) involve beam formed by pairs of lipped channel and Z-section profiles and (iii<sub>2</sub>) cover only small-to-moderate distortional slenderness values (from 0.68 to 1.53), “mingle” fairly well with those obtained in this work (*i.e.*, also follow the trend of a “Winter-type” curve) and exhibit a fairly small vertical dispersion.

Finally, Figs. 9(a)-(b) concern C120 P and F beams with  $\sigma_{y,20}=700\text{ MPa}$  and display their elastic-plastic equilibrium paths and the evolution of their deformed configurations and von Mises stress contours (before, at and beyond the peak load) – the 4 diagrams correspond to the equilibrium states indicated on the equilibrium path. It is worth noting that (i) the deformed configurations are amplified 3 times, and that (ii) state II always corresponds to the beam collapse (failure modes depicted). The observation of the results presented in these figures prompts the following remarks:

- (i) In both cases (P and F beams), yielding starts at the mid-span zone of the compressed lip free edge – see diagrams I. Collapse is also quite similar for both beams: it is associated with the full yielding of the web-flange corner at mid-span, leading to the formation of a “distortional plastic hinge” – see diagrams II, which also reveal that plasticity has already spread throughout the whole compressed lip mid-span zone – similar observations have been reported by Dinis and Camotim (2010).
- (ii) The compressed flange yields gradually along the equilibrium path descending branch – see diagrams III and IV. However, the spread of plasticity rate, after the onset of yielding, is much higher for the P-beams than for their F counterparts. Moreover, the stress diagrams IV indicate the occurrence of elastic unloading in mid-span compressed flange regions of the P (mostly) and F beams.



**Figure 9.** C120 (a) P and (b) F beam elastic and elastic-plastic equilibrium paths, deformed configurations (including the collapse mechanism) and von Mises stress contours ( $\sigma_{y,20}=700\text{ MPa}$ )

#### 4.4 DSM Design Considerations

This section addresses the applicability of the current Direct Strength Method (DSM) distortional design curve to predict the ultimate moments of the lipped channel beams analyzed in this work. It should be noted that the DSM was (i) originally proposed by Schafer and Peköz (1998), (ii) has been continuously improved since then, mostly due to the efforts of Schafer (2005, 2008), and (iii) was already included in Appendix 1 of the North American Specification for cold-formed steel structures (NAS 2007, 2012), but always in the context of room temperature. The nominal ultimate bending moment of cold-formed steel beams failing in distortional modes is given by the DSM equation/curve

$$M_{n,D} = M_{n,D,20} = \begin{cases} M_{y,20} & \text{for } \bar{\lambda}_{D,20} \leq 0.673 \\ M_{y,20} \left[ 1 - 0.22 \left( M_{cr,D,20} / M_{y,20} \right)^{0.5} \right] \left( M_{cr,D,20} / M_{y,20} \right)^{0.5} & \text{for } \bar{\lambda}_{D,20} > 0.673 \end{cases}, \quad (2)$$

where (i)  $M_{cr,D.20}$  and  $M_{y,20}$  are the beam distortional critical buckling and yield moments, and (ii) the beam distortional slenderness is defined as  $\bar{\lambda}_{D,20} = (M_{y,20}/M_{cr,D.20})^{0.5}$ .

Fig. 10(a) compares the current DSM distortional design curve with the numerical ultimate moment ratios displayed in Fig. 7(b), which were either obtained in this work (lipped channel beams – values in Tables A1 to A3 of the Annex A) or reported by Yu and Schafer (2007) (Z-section and lipped channel beams). Fig. 9(b), on the other hand, plots the ratios  $M_{n,D.20}/M_{u,20}$  against the distortional slenderness  $\bar{\lambda}_{D,20}$ , thus providing pictorial representations of the accuracy and safety of the DSM distortional ultimate moment estimates. The observation of these two figures leads to the following comments:

- (i) Naturally, the DSM design curve provides accurate and mostly safe predictions of the numerical (and experimental) distortional failure moments reported by Yu and Schafer (2007) – indeed, these failure moments were part of those used to develop/calibrate this design curve.
- (ii) Concerning the numerical ultimate moments obtained in this work, the DSM estimates are (ii<sub>1</sub>) mostly safe and accurate in the low-to-moderate slenderness range ( $\bar{\lambda}_{D,20} \leq 1.5$ ) and (ii<sub>2</sub>) clearly unsafe in the moderate-to-high slenderness range ( $\bar{\lambda}_{D,20} > 1.5$ ) – the overestimation tends to grow with  $\bar{\lambda}_{D,20}$  and is particularly severe for the most slender P-beams. These facts are reflected in the average, standard deviation and maximum/minimum values of the  $M_{n,D.20}/M_{u,20}$  ratios: 1.21, 0.36 and 2.32/0.84 – if only the beams with  $\bar{\lambda}_{D,20} \leq 1.5$  are considered, these indicators improve considerably and become 0.99, 0.09 and 1.22/0.84. At this stage, it should be recalled that all the numerical and experimental results reported by Yu and Schafer (2007), also used to calibrate/validate the current DSM distortional design curve (Schafer 2008), concern cold-formed steel (Z-section and lipped channel) beams with slenderness values comprised between 0.68 and 1.53.
- (iii) There is one exception to the content of the previous item: the C150 F-beam results, whose DSM estimates are fairly accurate in the whole slenderness range considered (slightly unsafe for the higher  $\bar{\lambda}_{D,20}$  values). Recall that the C150 F-beams exhibited higher post-buckling strength than their C120-160 counterparts (see Fig. 3(b)).
- (iv) The results of the limited parametric study carried out here provide evidence that the current DSM distortional strength/design curve overestimates, to a lesser or greater extent, practically the numerical ultimate moments concerning beams with  $\bar{\lambda}_{D,20} > 1.5$  ( $\bar{\lambda}_{D,20} > 1.2$ , to be more precise).

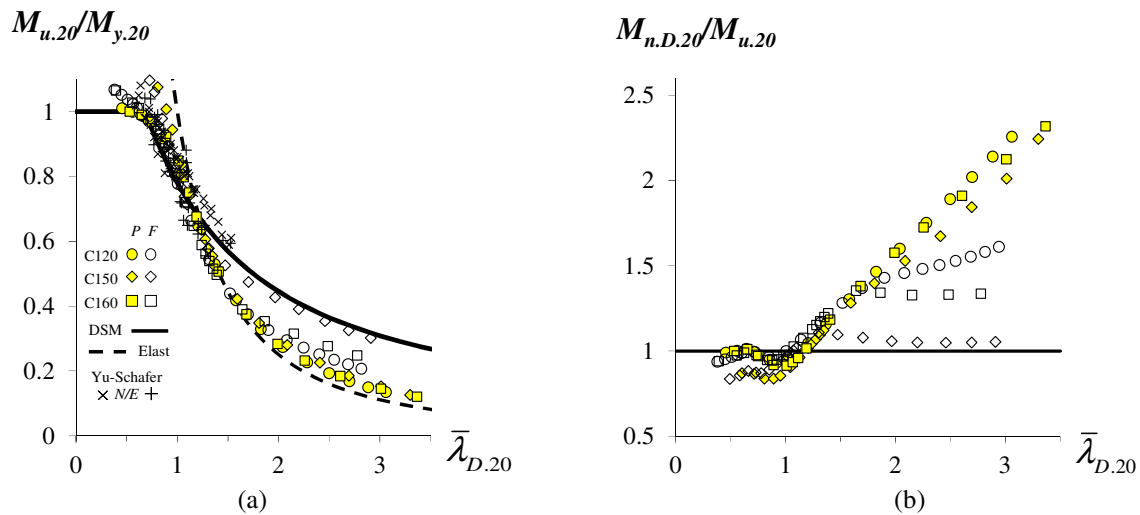


**Figure 10.** (a) Comparison between the current DSM distortional curve and F and P beams ultimate moments and (b)  $M_{n,D.20}/M_{u,20}$  values plotted against the distortional slenderness  $\bar{\lambda}_{D,20}$

## 5 Distortional Response under Elevated Temperature

### 5.1 Elastic-Plastic Post-Buckling Behavior

The influence of the (elevated) temperature on the distortional elastic-plastic post-buckling and ultimate strength behaviors of cold-formed steel simply supported lipped channel beams is investigated in this section. The investigation deals exclusively with P-beams and is based on the temperature-dependent steel constitutive law prescribed in EC3-1.2 (2005). Figs. 11(a)-(c) show the non-linear equilibrium paths ( $M/M_{cr,D,20}$  vs.  $|\delta|/t$ ) of C120-C150-C160 beams exhibiting  $\sigma_{y,20}=700\text{ MPa}$  and under the temperatures  $T=20/100-200-300-400-500-600-700-800\text{ }^\circ\text{C}$  – the white circles identify the ultimate moments  $M_{u,T}$  and the room temperature curve is presented here again for comparative purposes. As for Fig. 12, it displays the deformed configurations and von Mises stress contours occurring at the collapse ( $M=M_{u,T}$ ) of the C120 beams with  $\sigma_{y,20}=700\text{ MPa}$  and subjected to the 4 temperatures ( $T=200-400-600-800\text{ }^\circ\text{C}$ ). The observation of these results prompts the following remarks:

- (i) Obviously, the various beam equilibrium paths “move down” as the temperature  $T$  rises, thus leading to lower ultimate moment values.
- (ii) Concerning Fig. 12, note that, since the thermal action effects are negligible (uniform temperature and free-to-deform beams), the distortional failure modes are virtually identical for the four beams, *i.e.*, they do not depend on the temperature. However, the corresponding von Mises stress contours are not qualitatively so similar, neither among themselves nor to the room temperature diagrams II shown in Fig. 9(a) – the spread of plasticity in the compressed flange associated with the formation of

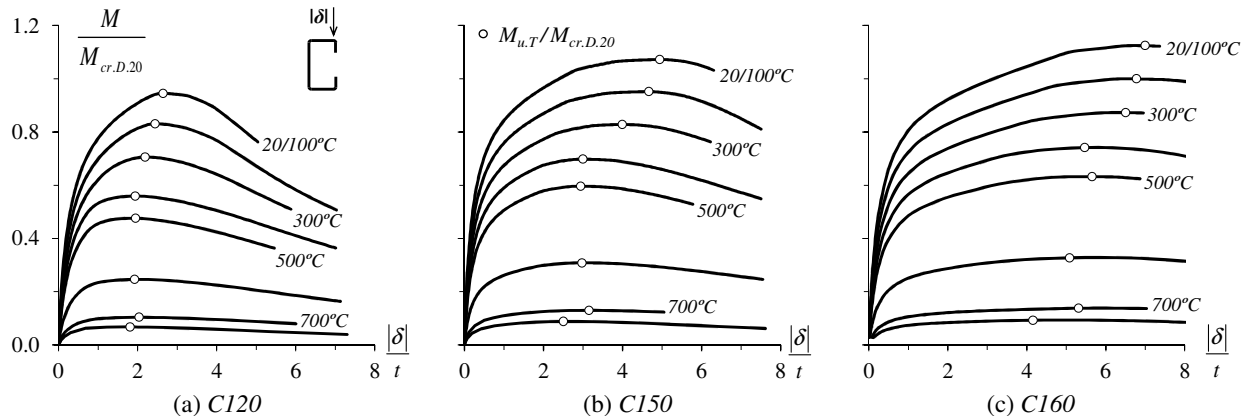


**Figure 11.** C120-C150-C160 P-beam distortional post-buckling equilibrium paths for  $\sigma_{y,20}=700\text{ MPa}$  and temperatures  $T=20/100-200-300-400-500-600-700-800\text{ }^\circ\text{C}$

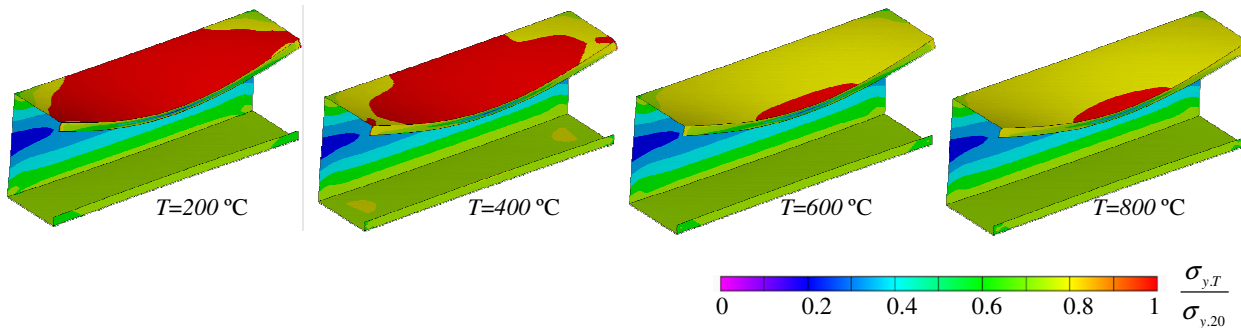


**Figure 12.** C120 beam deformed configurations and von Mises stress contours at distributions at collapse, for  $\sigma_{y,20}=700\text{ MPa}$  and temperatures  $T=200-400-600-800\text{ }^\circ\text{C}$

the “distortional plastic hinge” becomes less pronounced as  $T$  increases. This fact stems directly from the variation of the stress-strain-temperature curve shape – recall that  $k_p=0.81-0.42-0.18-0.05$  for  $T=200-400-600-800$ . Quantitatively speaking, the stresses obviously decrease as the temperature rises and continuously erodes the steel material behavior.

- (iii) The  $T \geq 600^\circ\text{C}$  curves are clearly apart and below their  $T \leq 500^\circ\text{C}$  counterparts (Fig. 11), which reflects the heavy degradation of the steel material behavior between  $500^\circ\text{C}$  and  $600^\circ\text{C}$ , namely via the proportionality limit strain and smoothness of the (elliptic) transition between the elastic and plastic ranges (see Fig. 2(b)) – for  $T \geq 600^\circ\text{C}$ , a the stress-strain curve has again a well-defined yield plateau.
- (iv) No clear trend was detected concerning the influence of the temperature, geometry and/or steel grade on the amount of beam elastic-plastic strength reserve and ductility prior to failure<sup>15</sup>. Indeed, regardless of the temperature, all beams exhibit quite similar post-collapse behaviors (equilibrium path descending branches).
- (v) In order to quantify the beam ultimate moment erosion stemming from the rising temperature, Fig. 13 depicts the variation of the ultimate moment ratio  $M_{u,T}/M_{u,20}$  with  $T$  for the seven yield stresses considered for beam C120 – solid lines. Also shown in this figure is the variation of the critical

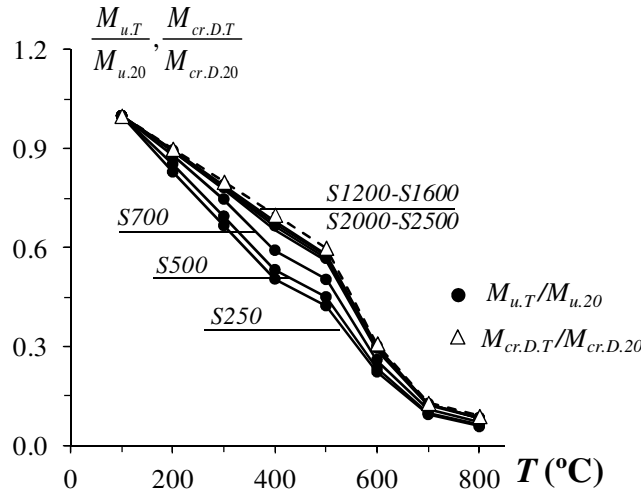


**Figure 13.** Variation of  $M_{u,T}/M_{u,20}$  (solid curves) and  $M_{cr,D,T}/M_{cr,D,20}$  with  $T$  (dashed curve) for C120 beams with  $\sigma_{y,20}=250-500-700-1200-1600-2000-2500\text{ MPa}$

**Table 5.**  $M_{u,T}/M_{cr,D,T}$  values concerning the C120 beams with  $\sigma_{y,20}=250-500-700-1200-1600-2000-2500\text{ MPa}$  under temperatures  $T=20/100-200-300-400-500-600-700-800^\circ\text{C}$

$T$ ( $^\circ\text{C}$ )	S250	S500	S700	S1200	S1600	S2000	S2500
20/100	0.50	0.84	0.94	1.04	1.10	1.14	1.18
200	0.47	0.80	0.92	1.03	1.09	1.13	1.17
300	0.42	0.73	0.88	1.01	1.07	1.12	1.16
400	0.36	0.64	0.80	0.98	1.04	1.10	1.15
500	0.36	0.63	0.79	0.97	1.04	1.09	1.14
600	0.36	0.64	0.79	0.98	1.05	1.10	1.15
700	0.37	0.64	0.80	0.98	1.05	1.11	1.16
800	0.33	0.59	0.75	0.95	1.02	1.06	1.11

<sup>15</sup> All the computed  $|\delta|/t$  values corresponding to the ultimate moments  $M_{u,T}$  are included in Tables B1 to B3 of the Annex.



moment ratio  $M_{cr,D,T}/M_{cr,D,20}$  with  $T$  – dashed line. On the other hand, Table 5 gives the  $M_{u,T}/M_{cr,D,T}$  values, which quantify the amount of post-critical strength reserve exhibited by each C120 beam. The analysis of these results leads to the following conclusions:

- (v.1) Obviously, the variation of  $M_{cr,D,T}/M_{cr,D,20}$  with  $T$  is the same for all yield stresses – recall that  $M_{cr,D,T}$  depends exclusively on the Young’s modulus reduction due to  $T$  (see Fig. 2(a)).
- (v.2) Since the ultimate moment variation is also affected by the ( $v_1$ ) proportionality limit and yield stresses, and ( $v_2$ ) the shape of the stress-strain curve, there is a clear dependence on  $T$ .
- (v.3) For the beams with  $\sigma_{y,20}=1600-2000-2500$  MPa, the critical and ultimate moment ratios practically coincide, which means that, at least for this particular C120 beam geometry, the (distortional) critical and ultimate moments are equally affected by the temperature. Indeed, the  $M_{u,T}/M_{cr,D,T}$  values are all very similar, even if they decrease slightly with  $T$  – they vary from 1.02 to 1.10 ( $\sigma_{y,20}=1600$  MPa), 1.09 to 1.14 ( $\sigma_{y,20}=2000$  MPa), and 1.11 to 1.18 ( $\sigma_{y,20}=2500$  MPa), thus indicating very similar post-critical strength reserves.
- (v.4) As the yield stress decreases, the beam critical moment ratios progressively fall below their ultimate moment counterparts, which means that (again for this particular beam geometry) the  $M_{u,T}/M_{cr,D,T}$  values decrease more significantly with  $T$  – Table 5 shows that this ratio falls by about 6% ( $\sigma_{y,20}=2500$  MPa), 8% ( $\sigma_{y,20}=2000-1600$  MPa), 10% ( $\sigma_{y,20}=1200$  MPa), 26% ( $\sigma_{y,20}=700$  MPa), 43% ( $\sigma_{y,20}=500$  MPa) and 55% ( $\sigma_{y,20}=250$  MPa).
- (v.5) The  $M_{u,T}/M_{cr,D,T}$  increase with the yield stress grows with  $T$  – it varies between about 67% ( $T=100$  °C) and 79% ( $T=800$  °C).
- (v.6) All the  $M_{u,T}/M_{cr,D,T}$  values concerning the beams with  $\sigma_{y,20}=250-500-700$  MPa are below 1.0, which means that their collapses occur before the critical applied stress level is reached. Moreover, those values decrease with both the temperature and the yield stress, thus implying that plasticity effects play an increasing role in beam failure.

## 5.2 Ultimate Moments

This section presents and discusses the results of the parametric study carried out to gather ultimate strength data that will make it possible to assess the quality of DSM ultimate moment estimates at elevated temperatures. This parametric study involved a total of 168 beams, corresponding to all possible combinations of the (i) three lipped channel geometries selected (C120-C150-C160), (ii) eight uniform temperatures ( $T=20/100-200-300-400-500-600-700-800$  °C)<sup>16</sup> and, (iii) seven room temperature yield stresses ( $\sigma_{y,20}=250-500-700-1200-1600-2000-2500$  MPa) – values covering wide distortional slenderness ranges:  $\lambda_{D,T}$  varies from 0.636 to 3.76. Tables B1 to B3, included in Annex B, provide the numerical (ANSYS SFEA) beam ultimate moments obtained in this investigation. Each table concerns one beam geometry (C120-C150-C160) and has information about (i) yield stresses and temperatures considered, (ii) the temperature-dependent yield moments  $M_{y,T}$  and distortional critical buckling moments  $M_{cr,D,T}$  (and distortional slenderness values  $\lambda_{D,T}$ ), (v) the computed ultimate moments  $M_{u,T}$  and associated  $(\delta/t)_{lim}$  values, and (iv) the ultimate moment ratios  $M_{u,T}/M_{y,T}$ . Fig. 14 plots eight sets of ultimate moment ratios  $M_{u,T}/M_{y,T}$  (one per temperature value) against the beam distortional slenderness  $\lambda_{D,T}$ . The observation of these plots makes it possible to conclude that the  $M_{u,T}/M_{y,T}$  vs.  $\lambda_{D,T}$  “clouds” follow trends that, apparently, can be described by “Winter-type” strength/design curves, which provides promising indications about the possibility and developing a DSM approach to predict them efficiently (safely and accurately) – this issue will be addressed in the next section.

<sup>16</sup> Note that 21 P-beam results concerning 20/100 °C (room temperature) have already been discussed in section 4. They are presented here again for comparison proposes.

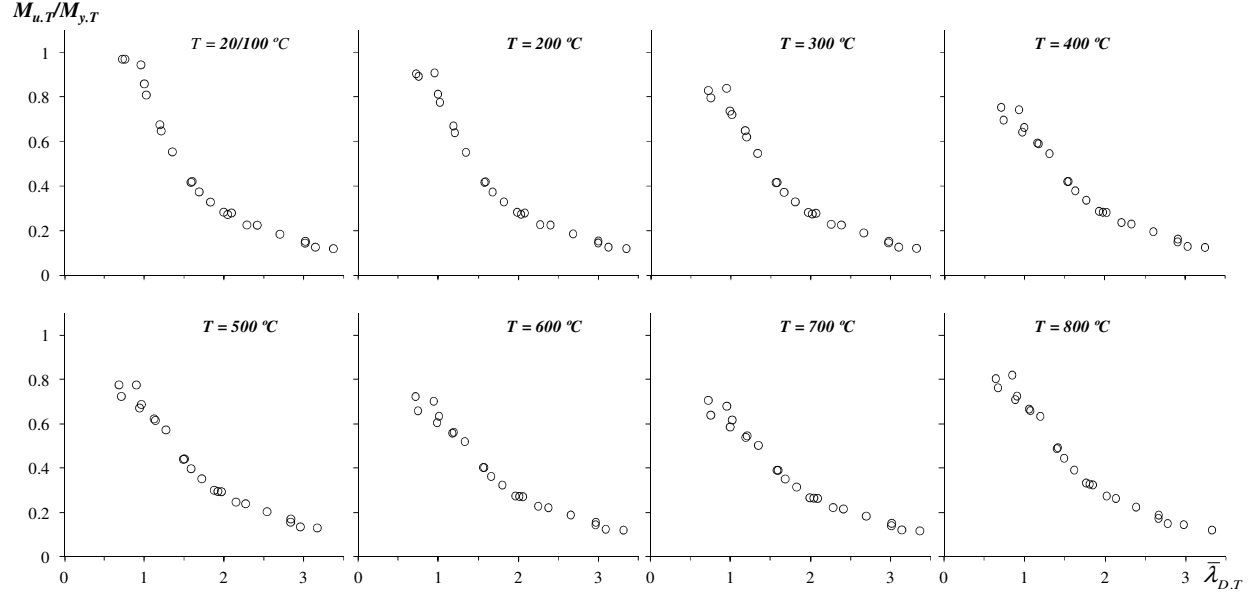


**Figure 14.** Numerical ultimate moment ratios  $M_{u,T}/M_{y,T}$  plotted against the beam distortional slenderness  $\bar{\lambda}_{D,T}$  for the C120-C150-C160 beams under temperatures  $T=20/100-200-300-400-500-600-700-800$  °C

### 5.3 DSM Design Considerations

Finally, this section address the adequacy of the current Direct Strength Method (DSM) distortional strength/design curve to predict the ultimate moment strength of the cold-formed steel lipped channel P-beams analyzed in this work, which (i) fail in distortional modes at elevated temperatures and (ii) exhibit the temperature-dependent steel constitutive behavior prescribed in EC3-1.2 – in particular, it is intended to assess whether the quality of the DSM ultimate moment estimates is affected by this temperature-dependency. The approach followed in this work, which has already (partially) been explored by other researchers, namely Chen and Young (2006, 2007b, 2008), Ranawaka and Mahendran (2009b) and Landesmann and Camotim (2010a,b, 2011, 2012a,b), consists of modifying Eq. (2) in order to account for the influence of the temperature on  $M_{cr,D}$  and  $M_y$ . This influence is felt through the Young's modulus and yield stress values, which are progressively reduced as the temperature (caused by fire conditions) increases. In other words,  $M_{cr,D}$  and  $M_y$  (or  $\sigma_y$ ) are replaced by  $M_{cr,D,T}$  and  $M_{y,T}$  (or  $\sigma_{y,T}$ ), which implies that that  $\bar{\lambda}_{D,T}$  also varies with  $T$ . In this framework, the nominal ultimate moment of cold-formed steel beams failing in distortional modes is given by the expressions

$$M_{n,D,T} = \begin{cases} M_{y,T} & \text{for } \bar{\lambda}_{D,T} \leq 0.673 \\ M_{y,T} \left[ 1 - 0.22 \left( M_{cr,D,T} / M_{y,T} \right)^{0.5} \right] \left( M_{cr,D,T} / M_{y,T} \right)^{0.5} & \text{for } \bar{\lambda}_{D,T} > 0.673 \end{cases}, \quad (3)$$

where (i)  $M_{cr,D,T}$  and  $M_{y,T}$  are the beam distortional critical buckling and yield moments, and (ii) the beam distortional slenderness is given by  $\bar{\lambda}_{D,T} = (M_{y,T} / M_{cr,D,T})^{0.5}$ .

Fig. 15 compares the modified current DSM distortional strength curve (solid line) with the numerical ultimate moment ratios obtained in this work – also included, for comparison purposes, is the elastic buckling strength curve (dashed line). Each plot concerns a different temperature ( $T=20/100-200-300-400-500-600-700-800$  °C) and the numerical  $M_{u,T}/M_{y,T}$  values were obtained from the analyses of P-beams with C120-C150-C160 geometries and the room temperature yield stresses  $\sigma_{y,20}=250-500-$

700-1200-1600-2000-2500 MPa – Tables B1 to B3, included in Annex B, supply the (i) DSM ultimate moment estimates  $M_{n,D,T}$  and (ii) ratios  $M_{n,D,T}/M_{u,T}$  and  $M_{n,D,T}/M_{y,T}$ . As for Fig. 16, it displays  $M_{n,D,T}/M_{u,T}$  vs.  $\bar{\lambda}_{D,T}$  plots that enable a quick assessment of the quality (accuracy and safety) of the modified DSM ultimate moment estimates in predicting beam distortional failures at elevated temperatures. The observation of the results presented in Figs. 15 and 16 makes it possible to conclude that:

- (i) The only accurate and safe ultimate moment predictions concern the stockier beams under room temperature or elevated temperatures not exceeding 200 °C.

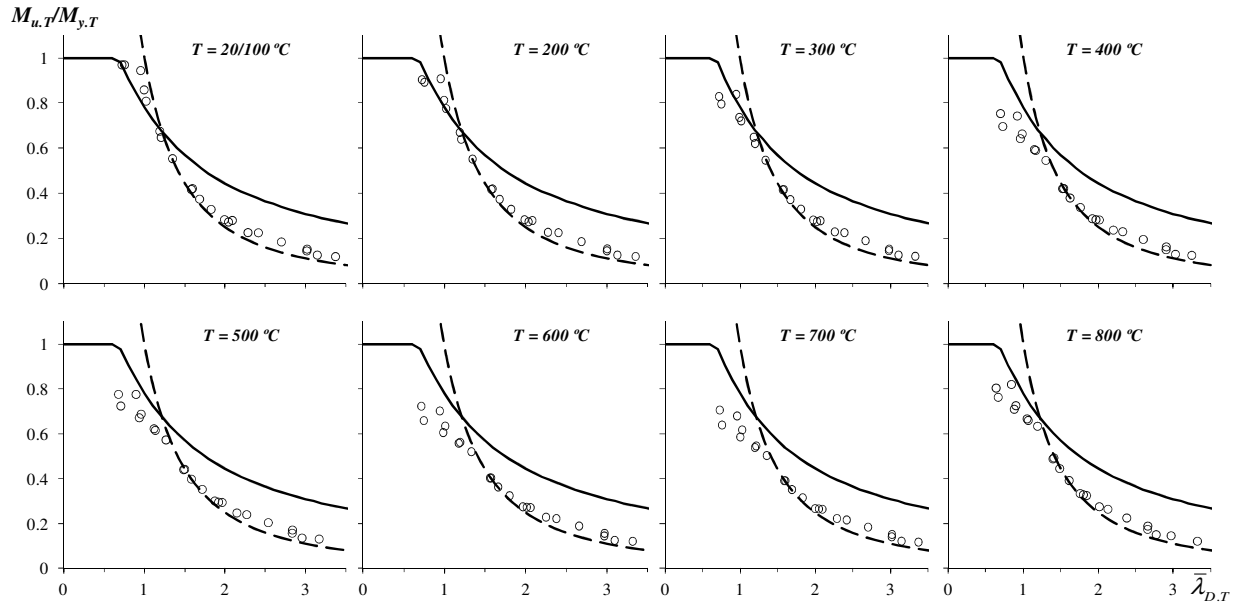


**Figure15.** Comparison between the modified current DSM distortional curve and the numerical beam ultimate moments at temperatures  $T=20/100-200-300-400-500-600-700-800$  °C

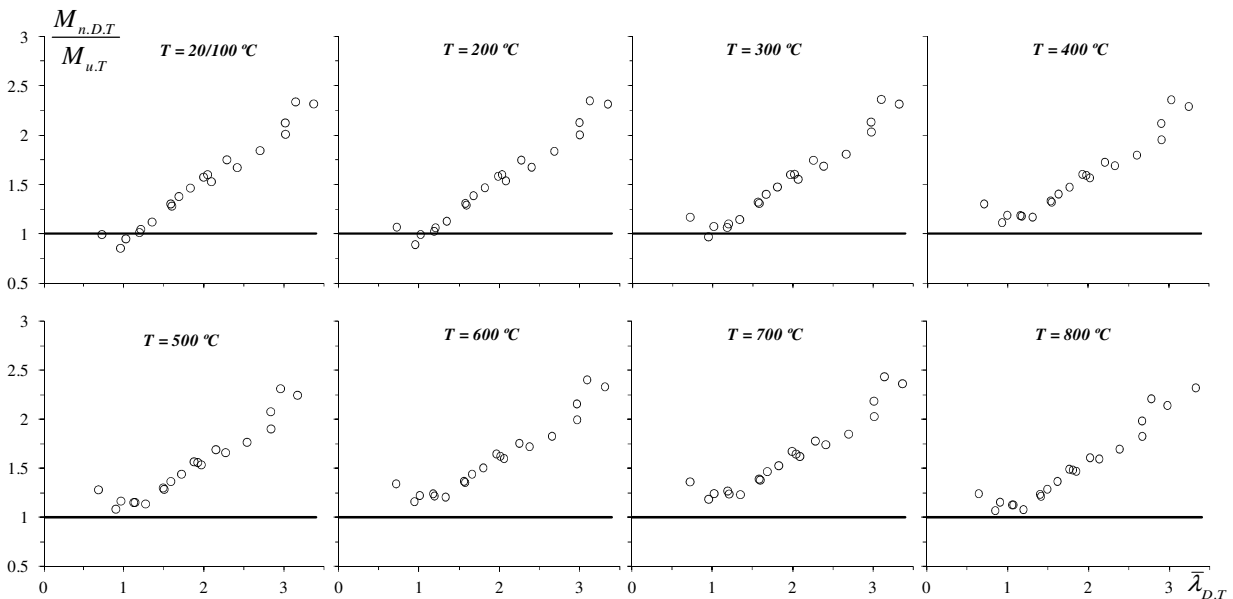


**Figure16.**  $M_{n,D,T}/M_{u,T}$  ratios plotted against the distortional slenderness  $\bar{\lambda}_{D,T}$  at temperatures  $T=20/100-200-300-400-500-600-700-800$  °C

- (ii) The ultimate moments of all the remaining beams are overestimated by an amount that grows very rapidly with the distortional slenderness  $\bar{\lambda}_{D,T}$  (see Fig. 16). Moreover, this overestimation does not appear to be influenced by either the cross-section geometry or the temperature value.
- (iii) It is rather interesting to note that, for  $\bar{\lambda}_{D,T} > 1.25$  and regardless of the cross-section dimensions or temperature value, the  $M_{u,T}/M_{y,T}$  ratios are quite nicely “aligned” with the elastic buckling strength curve. Naturally, the same does occur for the stockier beams ( $\bar{\lambda}_{D,T} \leq 1.25$ ), as the  $M_{u,T}/M_{y,T}$  ratios at room temperature (or  $T \leq 100^\circ\text{C}$ ) are the only ones remaining closely aligned with the elastic buckling strength curve. All the ratios concerning beams subjected to elevated temperatures ( $T > 100^\circ\text{C}$ ) are below that strength curve – the overestimation grows gradually with  $T$  up until  $T = 500^\circ\text{C}$  and remains fairly constant for higher temperatures.
- (iv) The findings described in the previous items strongly suggest that Eq. (3) needs to be modified, in order to achieve a satisfactory DSM prediction of the numerical beam ultimate moments obtained in this work. Apparently, the elastic buckling strength curves provides a good starting point for the required modifications – hopefully, this positive forecast will be confirmed by future research.

## 6 Concluding Remarks

This paper reported the available results of an ongoing numerical (ANSYS SFEA) investigation on the distortional post-buckling behavior, ultimate strength and design of cold-formed steel beams. These results concerned simply supported single-span lipped channel beams (i) displaying three geometries (cross-section dimensions and lengths), chosen to ensure pure distortional buckling and failure modes, (ii) exhibiting several room-temperature yield stresses, selected to cover a wide distortional slenderness range, and (iii) under various uniform temperature distributions caused by fire conditions (up to  $800^\circ\text{C}$ ). The final goal of this research effort is (i) to acquire in-depth knowledge on the influence of elevated temperatures on the distortional post-buckling and ultimate strength behaviors of cold-formed steel beams, and (ii) contribute towards the development and validation of an efficient DSM design approach for such members.

After selecting the beam cross-section dimensions and lengths chosen ensuring pure distortional buckling and failure modes and before addressing the influence of the elevated temperatures, it was necessary to validate the ANSYS shell finite element model employed to perform the intended investigation. In the context of this validation procedure, basically consisted of replicating numerical results obtained by Yu and Schafer (2007) for lipped channel beams subjected to four-point bending, a fairly insightful study on the distortional post-buckling behavior, ultimate strength and DSM design of cold-formed steel beams at room temperature was carried out. It involved the analysis of 110 simply supported single-span lipped channel beams with two end support conditions, differing in the warping displacement and local displacement/rotation restraints. The main output of this limited parametric study was the finding that the current DSM strength/design curve only provides safe and accurate ultimate moment estimates in the low-to-moderate slenderness range ( $\bar{\lambda}_{D,20} \leq 1.5$ ) – all the beams numerically analyzed by Yu and Schafer (2007) fell in this range. For more slender beams ( $\bar{\lambda}_{D,20} > 1.5$ ), the DSM ultimate moment estimates were shown to considerably overestimate the numerical values, particularly when the end support warping displacement and local displacements/rotations are free. This issue deserves further investigation, which is planned for the near future.

The investigation on cold-formed steel beams subjected to elevated temperatures dealt exclusively with single-span lipped channel beams with free warping displacement and local displacements/rotations at the end cross-sections (P-beams). The ultimate moments of 168 lipped channel beams, containing critical-

mode initial geometrical imperfections and combining three geometries, seven yield stresses and eight temperature values, were calculated and compared with their estimates provided a modification of the DSM distortional strength curve, to accommodate for the variation of the critical buckling and yield moments with the temperature, according to temperature-dependent steel constitutive law prescribed in EC3-1.2. This comparison showed that:

- (i) With very few exceptions, all concerning stocky beams under moderate temperatures, the ultimate moments were found to be clearly overestimated by the modified DSM estimates, with the amount of the overestimation growing very rapidly with the distortional slenderness.
- (ii) For  $\bar{\lambda}_{D,T} > 1.25$  and regardless of the cross-section dimensions or temperature value, the ultimate moments were quite accurately predicted by the elastic buckling strength curve. This rather surprising positive feature deserves to be further explored in the future.

Finally, one last word to mention that the authors are currently extending the scope of this investigation to other (i) beam geometries (cross-section shape/dimensions and lengths), (ii) end support conditions, and (iii) other available experimentally-based temperature-dependent constitutive models, namely those proposed by Chen and Young (2007a), Ranawaka and Mahendran (2009a), Kankaname and Mahendran (2011), Wei and Jihong (2012) and Silva *et al.* (2014). The corresponding results, which will be used to either confirm or supplement the findings obtained in this work, should be reported in the near future.

## References

- ABNT (2010). Brazilian Standard on Design of Cold-Formed Steel Structures (ABNT NBR 14762:2010), Brazilian Standards Association, Rio de Janeiro, RJ. (Portuguese)
- Abreu JCB, Schafer BW (2013). Stability of cold-formed steel compression members under thermal gradients, *USB Proceedings of SSRC Annual Stability Conference* (St. Louis, 17-19/4).
- Andreassen MJ, Jönsson J (2013). A distortional semi-discretized thin-walled beam element, *Thin-Walled Structures*, **62**(January), 142-157.
- AS/NZS (2005). *Cold-Formed Steel Structures*, Standards of Australia (SA) and Standards of New Zealand (SNZ), Sydney-Wellington.
- Bebiano R, Pina P, Silvestre N, Camotim D (2008a). *GBTUL 1.0 $\beta$  – Buckling and Vibration Analysis of Thin-Walled Members*, DECivil/IST, Technical University of Lisbon. (<http://www.civil.ist.utl.pt/gbt>)
- Bebiano R, Silvestre N, Camotim D (2008b). *GBTUL – A code for the buckling analysis of cold-formed steel members*”, *Proceedings of 19<sup>th</sup> International Specialty Conference on Recent Research and Developments in Cold-Formed Steel Design and Construction* (St. Louis, 14-15/10), R LaBoube, WW Yu (eds.), 61-79.
- Chen J, Young B (2006). Corner properties of cold-formed steel sections at elevated temperatures, *Thin-Walled Structures*, **44**(2), 216-223.
- Chen J, Young B (2007a). Experimental investigation of cold-formed steel material at elevated temperatures. *Thin-Walled Structures*, **45**(1), 96-110.
- Chen J, Young B (2007b). Cold-formed steel lipped channel columns at elevated temperatures, *Engineering Structures*, **29**(10), 2445-2456.
- Chen J, Young B (2008). Design of high strength steel columns at elevated temperatures, *Journal of Constructional Steel Research*, **64**(6), 689-703.
- Chen W, Ye J, Bai Y, Zhao XL (2012). Full-scale fire experiments on load-bearing cold-formed steel walls lined with different panels, *Journal of Constructional Steel Research*, **79**(Dec), 242-254.
- Chen W, Ye J, Bai Y, Zhao XL (2013). Improved fire resistant performance of load bearing cold-formed steel interior and exterior wall systems, *Thin-Walled Structures*, **73**(Dec), 145-157
- Dinis PB, Camotim D (2010). Local/distortional mode interaction in cold-formed steel lipped channel beams, *Thin-Walled Structures*, **48**(10-11), 771-785.

- EC3-1.2 (2005). *Eurocode 3: Design of Steel Structures – Part 1-2: General Rules – Structural Fire Design*, Comité Européen de Normalisation (CEN), Brussels.
- Ellobody E (2013). A consistent nonlinear approach for analysing steel, cold-formed steel, stainless steel and composite columns at ambient and fire conditions, *Thin-Walled Structures*, **68**(July), 1-17.
- Feng M, Wang YC (2005a). An analysis of the structural behaviour of axially loaded full-scale cold-formed thin-walled steel structural panels tested under fire conditions, *Thin-Walled Structures*, **43**(2), 291-332.
- Feng M, Wang YC (2005b). An experimental study of loaded full-scale cold-formed thin-walled steel structural panels under fire conditions, *Fire Safety Journal*, **40**(1), 43-63.
- Feng M, Wang YC, Davies JM (2003a). Structural behaviour of cold-formed thin-walled short steel channel columns at elevated temperatures – Part 1: experiments, *Thin-Walled Structures*, **41**(6), 543-570.
- Feng M, Wang YC, Davies JM (2003b). Structural behaviour of cold-formed thin-walled short steel channel columns at elevated temperatures – Part 2: design calculations and numerical analysis, *Thin-Walled Structures*, **41**(6), 571-594.
- Feng M, Wang YC, Davies JM (2003c). Thermal performance of cold-formed thin-walled steel panel systems in fire, *Fire Safety Journal*, **38**(4), 365-394.
- Feng M, Wang YC, Davies JM (2003d). Axial strength of cold-formed thin-walled steel channels under non-uniform temperatures in fire, *Fire Safety Journal*, **38**(8), 679-707.
- Feng M, Wang YC, Davies JM (2004). A numerical imperfection sensitivity study of cold-formed thin-walled tubular steel columns at uniform elevated temperatures, *Thin-Walled Structures*, **42**(4), 533-555.
- Gunalan S, Kolarkar P, Mahendran M (2013). Experimental study of load bearing cold-formed steel wall systems under fire conditions, *Thin-Walled Structures*, **65**(April), 72-92.
- Gunalan S, Mahendran M (2013a). Finite element modelling of load bearing cold-formed steel wall systems under fire conditions, *Engineering Structures*, **56**(November), 1007-1027.
- Gunalan S, Mahendran M (2013b). Development of improved fire design rules for cold-formed steel wall systems, *Journal of Constructional Steel Research*, **88**(September), 339-362.
- Haidarali MR, Nethercot DA (2012). Local and distortional buckling of cold-formed steel beams with edge-stiffened flanges, *Journal of Constructional Steel Research*, **73**(June), 31-42.
- Kaitila O (2002). Imperfection sensitivity analysis of lipped channel columns at high temperatures, *Journal of Constructional Steel Research*, **58**(3), 333-51.
- Kalkan I, Buyukkaragoz A (2012). A numerical and analytical study on distortional buckling of doubly-symmetric steel I-beams, *Journal of Constructional Steel Research*, **70**(March), 289-297.
- Kankanamge ND, Mahendran M (2011). Mechanical properties of cold-formed steels at elevated temperatures, *Thin-Walled Structures*, **49**(1), 26-44.
- Kankanamge ND, Mahendran M (2012). Behaviour and design of cold-formed steel beams subject to lateral-torsional buckling at elevated temperatures, *Thin-Walled Structures*, **61**(December), 213-228.
- Laím L, Rodrigues JPC, Silva LS (2014). Experimental analysis on cold-formed steel beams subjected to fire, *Thin-Walled Structures*, **74**(January), 104-117.
- Landesmann A, Camotim D (2010a). Distortional failure and design of cold-formed steel lipped channel columns under fire conditions, *Proceedings of SSRC Annual Stability Conference* (Orlando, 12-15/5), 505-532.
- Landesmann A, Camotim D (2010b). Distortional failure and design of cold-formed steel rack-section columns under fire conditions, *Proceedings of Fourth International Conference on Steel & Composite Structures* (ICSCS'2011 – Sydney, 21-23/7), B. Uy *et al.* (eds.), 287-289. (full paper in CD-ROM Proceedings)
- Landesmann A, Camotim D (2011). On the distortional buckling, post-buckling and strength of cold-formed steel lipped channel columns under fire conditions, *Journal of Structural Fire Engineering*, **2**(1), 1-19.
- Landesmann A, Camotim D (2012a). Application of direct strength method design to distortional buckling resistance of thin-walled steel columns exposed to fire, *Proceedings of Eleventh International Conference on Computational Structures Technology* (CST 2012 – Dubrovnik, 4-7/9), BHV Topping. (ed.), Civil-Comp Press (Stirling), paper 30. (full paper in *USB Key Drive Proceedings* – doi:10.4203/ccp.99.30).
- Landesmann A, Camotim D (2012b). DSM design of cold-formed steel columns failing distortional exposed to fire: how relevant is the temperature dependence of the material behavior?, *USB Proceedings of the SSRC Annual Stability Conference* (Grapevine, 18-21/4).

- Landesmann A, Camotim D, Batista EM (2009). “On the distortional buckling, post-buckling and strength of cold-formed steel lipped channel columns subjected to elevated temperatures”, *Proceedings of International Conference on Applications of Structural Fire Engineering* (Prague – 19-20/2), F. Wald, P. Kallerová, J. Chlouba (eds.), A8-A13.
- Landesmann A, Camotim D, Basaglia C (2013). “Distortional post-buckling behavior and strength of cold-formed steel columns: how does the cross-section affect it?”, *USB Key Drive Proceedings of SSRC Annual Stability Conference* (St. Louis, 16-20/4).
- Lee JH, Mahendran M, Makelainen P (2003). Prediction of mechanical properties of light gauge steels at elevated temperatures, *Journal of Constructional Steel Research*, **59**(12), 1517-1532.
- Lim JBP, Young B (2007). Effects of elevated temperatures on bolted moment-connections between cold-formed steel members, *Engineering Structures*, **29**(10), 2419-2427.
- NAS (2012). *North American Specification for the Design of Cold-Formed Steel Structural Members* (AISI-S100-12), American Iron and Steel Institute (AISI), Washington, DC.
- Outinen J, Kaitila O, Makelainen P (2000). “A study for the development of the design of steel structures in fire conditions”, *Proceedings of First International Workshop on Structures in Fire* (SiF’2000 – Copenhagen, 19-20/6), JM Franssen (ed.), 267-281.
- Ranawaka T (2006). *Distortional Buckling Behaviour of Cold-Formed Steel Compression Members at Elevated Temperatures*, Ph.D. Thesis, Queensland University of Technology, Australia.
- Ranawaka T, Mahendran M (2009a). Experimental study of the mechanical properties of light gauge cold-formed steels at elevated temperatures, *Fire Safety Journal*, **44**(2), 219–229.
- Ranawaka T, Mahendran M (2009b). Distortional buckling tests of cold-formed steel compression members at elevated temperatures, *Journal of Constructional Steel Research*, **65**(2), 249-259.
- Ranawaka T, Mahendran M (2010). Numerical modelling of light gauge cold-formed steel compression members subjected to distortional buckling at elevated temperatures, *Thin-Walled Structures*, **48**(3-4), 334-344.
- SAS (Swanson Analysis Systems Inc.) (2009). *ANSYS Reference Manual* (version 12).
- Schafer BW (2000). *Distortional Buckling of Cold-Formed Steel Columns*, American Iron and Steel Institute (AISI) Report, Washington DC.
- Schafer BW (2005). *Direct Strength Method Design Guide*, American Iron and Steel Institute (AISI) Report, Washington DC.
- Schafer BW (2008). Review: the Direct Strength Method of cold-formed steel member design, *Journal of Constructional Steel Research*, **64**(7-8), 766-788.
- Schafer BW, Peköz T (1998). Direct strength prediction of cold-formed steel members using numerical elastic buckling solutions, *Proceedings of 14<sup>th</sup> International Specialty Conference on Cold-formed Steel Structures* (St. Louis, 15-16/10), R LaBoube, WW Yu (eds.), 69-76.
- Shahbazian A, Wang YC (2011a). Calculating the global buckling resistance of thin-walled steel members with uniform and non-uniform elevated temperatures under axial compression, *Thin-Walled Structures*, **49**(11), 1415-1428.
- Shahbazian A, Wang YC (2011b). Application of the Direct Strength Method to local buckling resistance of thin-walled steel members with non-uniform elevated temperatures under axial compression, *Thin-Walled Structures*, **49**(12), 1573-1583.
- Shahbazian A, Wang YC (2012). Direct Strength Method for calculating distortional buckling capacity of cold-formed thin-walled steel columns with uniform and non-uniform elevated temperatures, *Thin-Walled Structures*, **53**(April), 188-199.
- Shahbazian A, Wang YC (2013). A simplified approach for calculating temperatures in axially loaded cold-formed thin-walled steel studs in wall panel assemblies exposed to fire from one side, *Thin-Walled Structures*, **64**(March), 60-72.
- Shahbazian A, Wang YC (2014). A fire resistance design method for thin-walled steel studs in wall panel constructions exposed to parametric fires, *Thin-Walled Structures*, **77**(April), 67-76.
- Silva FCM, Landesmann A, Batista EM, Camotim D (2014). Experimental investigation of mechanical properties of ZAR-345 cold-formed steel at elevated temperatures, *submitted for publication*.
- Wei C, Jihong Y (2012). Mechanical properties of G550 cold-formed steel under transient and steady state conditions, *Journal of Constructional Steel Research*, **73**(June), 1-11.
- Yu C, Schafer BW (2007). Simulation of cold-formed steel beams in local and distortional buckling with applications to the direct strength method, *Journal of Constructional Steel Research*, **63**(5), 581-590.
- Zhao B, Kruppa J, Renaud C, O’Connor M, Mecozzi E *et al.* (2005), *Calculation Rules of Lightweight Steel Sections in Fire Situations*, EUR-21426 (Technical Steel Research Series) – Steel Products and Applications for Building, Construction and Industry, European Commission Technical Steel Research, Luxembourg.

## ANNEX A – DATA CONCERNING BEAMS AT ROOM TEMPERATURE

Tables A1 to A3 provide the numerical beam ultimate moments and their DSM estimates. Each table concerns one beam geometry (C120-C150-C160) and the two end support conditions considered (Pinned and Fixed), and provides information about the (i) steel yield stress  $\sigma_{y,20}$ , (ii) yield moment  $M_{y,20}$ , (iii) distortional slenderness  $\bar{\lambda}_{D,20}$ , (iv) numerical ultimate moment  $M_{y,20}$  and associated limit  $l\delta/t$  value, denoted  $(l\delta/t)_{\text{lim}}$ , (v) ultimate moment ratios  $M_{u,20}/M_{cr,D,20}$  and  $M_{u,20}/M_{y,20}$ , (vi) DSM ultimate moment estimates  $M_{n,D,20}$  and (vii) ratios  $M_{n,D,20}/M_{y,20}$  and  $M_{n,D,20}/M_{u,20}$ .



Table A1(I): Numerical ultimate loads and DSM estimates at room temperature concerning the C120 P-beams analyzed.

$\sigma_{y,20}$ (MPa)	$M_{y,20}$ (kN·cm)	$\bar{\lambda}_{D,20}$	$M_{u,20}$ (kN·cm)	$(\delta/t)_{lim}$	$\frac{M_{u,20}}{M_{cr,D,20}}$	$\frac{M_{u,20}}{M_{y,20}}$	$M_{n,D,20}$ (kN·cm)	$\frac{M_{n,D,20}}{M_{y,20}}$	$\frac{M_{n,D,20}}{M_{u,20}}$
100	372.40	0.46	376.19	100	0.21	1.01	372.40	1.00	0.99
150	558.59	0.56	558.25	150	0.31	1.00	558.59	1.00	1.00
200	744.79	0.65	735.80	200	0.41	0.99	744.79	1.00	1.01
250	930.99	0.72	902.95	250	0.50	0.97	896.85	0.96	0.99
350	1303.38	0.85	1195.95	350	0.67	0.92	1133.25	0.87	0.95
500	1861.98	1.02	1506.45	500	0.84	0.81	1431.29	0.77	0.95
700	2606.77	1.21	1689.15	700	0.94	0.65	1765.60	0.68	1.05
900	3351.56	1.37	1774.10	900	0.99	0.53	2054.67	0.61	1.16
1200	4468.74	1.58	1866.45	1200	1.04	0.42	2433.39	0.54	1.30
1600	5958.32	1.83	1960.45	1600	1.10	0.33	2870.69	0.48	1.46
2000	7447.90	2.04	2034.80	2000	1.14	0.27	3255.97	0.44	1.60
2500	9309.88	2.28	2105.40	2500	1.18	0.23	3686.72	0.40	1.75
3000	11171.85	2.50	2155.65	3000	1.21	0.19	4076.14	0.36	1.89
3500	13033.83	2.70	2195.30	3500	1.23	0.17	4434.26	0.34	2.02
4000	14895.81	2.89	2228.20	4000	1.25	0.15	4767.58	0.32	2.14
4500	16757.78	3.06	2251.65	4500	1.26	0.13	5080.65	0.30	2.26

Table A1(II): Numerical ultimate loads and DSM estimates at room temperature concerning the C120 F-beams analyzed.

$\sigma_{y,20}$ (MPa)	$M_{y,20}$ (kN·cm)	$\bar{\lambda}_{D,20}$	$M_{u,20}$ (kN·cm)	$(\delta/t)_{lim}$	$\frac{M_{u,20}}{M_{cr,D,20}}$	$\frac{M_{u,20}}{M_{y,20}}$	$M_{n,D,20}$ (kN·cm)	$\frac{M_{n,D,20}}{M_{y,20}}$	$\frac{M_{n,D,20}}{M_{u,20}}$
100	372.40	0.38	397.72	0.51	0.15	1.07	372.40	1.00	0.94
140	521.35	0.45	548.45	0.65	0.21	1.05	521.35	1.00	0.95
180	670.31	0.51	695.10	0.79	0.27	1.04	670.31	1.00	0.96
220	819.27	0.56	838.35	0.90	0.32	1.02	819.27	1.00	0.98
250	930.99	0.60	943.05	0.99	0.37	1.01	930.99	1.00	0.99
350	1303.38	0.71	1271.55	1.28	0.49	0.98	1266.26	0.97	1.00
500	1861.98	0.85	1682.25	2.16	0.65	0.90	1624.31	0.87	0.97
700	2606.77	1.01	2027.00	3.59	0.79	0.78	2025.92	0.78	1.00
900	3351.56	1.14	2224.50	4.51	0.86	0.66	2373.20	0.71	1.07
1200	4468.74	1.32	2428.40	5.63	0.94	0.54	2828.16	0.63	1.16
1600	5958.32	1.52	2616.85	6.57	1.01	0.44	3353.51	0.56	1.28
2000	7447.90	1.70	2788.05	8.30	1.08	0.37	3816.35	0.51	1.37
2500	9309.88	1.90	3033.30	10.70	1.18	0.33	4333.82	0.47	1.43
3000	11171.85	2.08	3296.20	12.08	1.28	0.30	4801.65	0.43	1.46
3500	13033.83	2.25	3534.10	13.21	1.37	0.27	5231.86	0.40	1.48
4000	14895.81	2.40	3746.10	14.18	1.45	0.25	5632.30	0.38	1.50
4500	16757.78	2.55	3933.80	14.93	1.52	0.23	6008.39	0.36	1.53
5000	18619.76	2.69	4099.20	15.82	1.59	0.22	6364.11	0.34	1.55
5500	20481.73	2.82	4239.20	16.59	1.64	0.21	6702.45	0.33	1.58
6000	22343.71	2.94	4360.20	17.01	1.69	0.20	7025.72	0.31	1.61

Table A2(I): Numerical ultimate loads and DSM estimates at room temperature concerning the C150 P-beams analyzed.

$\sigma_{y,20}$ (MPa)	$M_{y,20}$ (kN·cm)	$\bar{\lambda}_{D,20}$	$M_{u,20}$ (kN·cm)	$(\delta/t)_{lim}$	$\frac{M_{u,20}}{M_{cr,D,20}}$	$\frac{M_{u,20}}{M_{y,20}}$	$M_{n,D,20}$ (kN·cm)	$\frac{M_{n,D,20}}{M_{y,20}}$	$\frac{M_{n,D,20}}{M_{u,20}}$
100	372.40	0.38	397.72	0.51	0.15	1.07	372.40	1.00	0.94
140	521.35	0.45	548.45	0.65	0.21	1.05	521.35	1.00	0.95
180	670.31	0.51	695.10	0.79	0.27	1.04	670.31	1.00	0.96
220	819.27	0.56	838.35	0.90	0.32	1.02	819.27	1.00	0.98
250	930.99	0.60	943.05	0.99	0.37	1.01	930.99	1.00	0.99
350	1303.38	0.71	1271.55	1.28	0.49	0.98	1266.26	0.97	1.00
500	1861.98	0.85	1682.25	2.16	0.65	0.90	1624.31	0.87	0.97
700	2606.77	1.01	2027.00	3.59	0.79	0.78	2025.92	0.78	1.00
900	3351.56	1.14	2224.50	4.51	0.86	0.66	2373.20	0.71	1.07
1200	4468.74	1.32	2428.40	5.63	0.94	0.54	2828.16	0.63	1.16
1600	5958.32	1.52	2616.85	6.57	1.01	0.44	3353.51	0.56	1.28
2000	7447.90	1.70	2788.05	8.30	1.08	0.37	3816.35	0.51	1.37

Table A2(II): Numerical ultimate loads and DSM estimates at room temperature concerning the C150 F-beams analyzed.

$\sigma_{y,20}$ (MPa)	$M_{y,20}$ (kN·cm)	$\bar{\lambda}_{D,20}$	$M_{u,20}$ (kN·cm)	$(\delta/t)_{lim}$	$\frac{M_{u,20}}{M_{cr,D,20}}$	$\frac{M_{u,20}}{M_{y,20}}$	$M_{n,D,20}$ (kN·cm)	$\frac{M_{n,D,20}}{M_{y,20}}$	$\frac{M_{n,D,20}}{M_{u,20}}$
100	691.85	0.49	827.30	0.59	0.29	1.20	691.85	1.00	0.84
140	968.58	0.58	1129.80	0.74	0.40	1.17	968.58	1.00	0.86
180	1245.32	0.66	1412.85	0.87	0.49	1.13	1245.32	1.00	0.88
220	1522.06	0.73	1669.00	1.14	0.58	1.10	1456.88	0.96	0.87
250	1729.61	0.78	1834.05	1.53	0.64	1.06	1594.53	0.92	0.87
300	2075.54	0.85	2030.90	1.82	0.71	0.98	1806.73	0.87	0.89
350	2421.46	0.92	2172.95	2.20	0.76	0.90	2001.86	0.83	0.92
400	2767.38	0.98	2289.20	2.58	0.80	0.83	2183.49	0.79	0.95
425	2940.34	1.01	2340.00	2.75	0.82	0.80	2270.04	0.77	0.97
450	3113.31	1.04	2384.90	2.90	0.83	0.77	2354.08	0.76	0.99
475	3286.27	1.07	2426.80	3.05	0.85	0.74	2435.82	0.74	1.00
500	3459.23	1.10	2467.15	3.29	0.86	0.71	2515.43	0.73	1.02
700	4842.92	1.30	2792.00	4.99	0.98	0.58	3091.48	0.64	1.11
900	6226.61	1.48	3275.65	9.64	1.15	0.53	3589.59	0.58	1.10
1200	8302.15	1.70	3936.40	10.72	1.38	0.47	4242.16	0.51	1.08
1600	11069.53	1.97	4725.80	12.17	1.65	0.43	4995.68	0.45	1.06
2000	13836.92	2.20	5394.00	13.54	1.89	0.39	5659.55	0.41	1.05
2500	17296.14	2.46	6109.90	14.65	2.14	0.35	6401.78	0.37	1.05
3000	20755.37	2.69	6740.30	15.65	2.36	0.32	7072.80	0.34	1.05
3500	24214.60	2.91	7297.40	16.49	2.55	0.30	7689.88	0.32	1.05

Table A3(I): Numerical ultimate loads and DSM estimates at room temperature concerning the C160 P-beams analyzed.

$\sigma_{y,20}$ (MPa)	$M_{y,20}$ (kN·cm)	$\bar{\lambda}_{D,20}$	$M_{u,20}$ (kN·cm)	$( \delta /l)_{lim}$	$\frac{M_{u,20}}{M_{cr,D,20}}$	$\frac{M_{u,20}}{M_{y,20}}$	$M_{n,D,20}$ (kN·cm)	$\frac{M_{n,D,20}}{M_{y,20}}$	$\frac{M_{n,D,20}}{M_{u,20}}$
50	238.44	0.53	238.34	0.23	0.28	1.00	238.44	1.00	1.00
75	357.66	0.65	354.18	0.45	0.42	0.99	357.66	1.00	1.01
100	476.87	0.75	462.55	0.62	0.55	0.97	448.39	0.94	0.97
140	667.62	0.89	615.35	1.04	0.73	0.92	564.48	0.85	0.92
180	858.37	1.01	728.75	1.94	0.87	0.85	664.86	0.77	0.91
200	953.75	1.06	760.50	2.41	0.90	0.80	710.84	0.75	0.93
220	1049.12	1.12	787.35	2.39	0.94	0.75	754.57	0.72	0.96
250	1192.19	1.19	805.40	2.86	0.96	0.68	816.60	0.68	1.01
350	1669.06	1.41	844.80	3.78	1.00	0.51	1000.15	0.60	1.18
500	2384.37	1.68	892.80	5.15	1.06	0.37	1231.56	0.52	1.38
700	3338.12	1.99	946.60	7.00	1.12	0.28	1491.13	0.45	1.58
900	4291.87	2.26	994.45	8.33	1.18	0.23	1715.58	0.40	1.73
1200	5722.49	2.61	1051.80	9.58	1.25	0.18	2009.64	0.35	1.91
1600	7629.99	3.01	1105.80	11.74	1.31	0.14	2349.18	0.31	2.12
2000	9537.49	3.37	1142.80	14.20	1.36	0.12	2648.32	0.28	2.32

Table A3(II): Numerical ultimate loads and DSM estimates at room temperature concerning the C160 F-beams analyzed.

$\sigma_{y,20}$ (MPa)	$M_{y,20}$ (kN·cm)	$\bar{\lambda}_{D,20}$	$M_{u,20}$ (kN·cm)	$( \delta /l)_{lim}$	$\frac{M_{u,20}}{M_{cr,D,20}}$	$\frac{M_{u,20}}{M_{y,20}}$	$M_{n,D,20}$ (kN·cm)	$\frac{M_{n,D,20}}{M_{y,20}}$	$\frac{M_{n,D,20}}{M_{u,20}}$
40	190.75	0.39	203.21	0.62	0.16	1.07	190.75	1.00	0.94
80	381.50	0.56	391.97	0.96	0.32	1.03	381.50	1.00	0.97
100	476.87	0.62	481.93	1.08	0.39	1.01	476.87	1.00	0.99
140	667.62	0.73	652.40	1.37	0.53	0.98	636.48	0.95	0.98
180	858.37	0.83	799.75	1.89	0.65	0.93	758.10	0.88	0.95
200	953.75	0.88	861.30	2.55	0.70	0.90	813.82	0.85	0.94
220	1049.12	0.92	912.45	3.15	0.74	0.87	866.81	0.83	0.95
250	1192.19	0.98	966.00	3.36	0.78	0.81	941.98	0.79	0.98
300	1430.62	1.08	1030.80	4.27	0.83	0.72	1057.84	0.74	1.03
350	1669.06	1.16	1080.85	4.93	0.87	0.65	1164.38	0.70	1.08
400	1907.50	1.24	1121.25	5.30	0.91	0.59	1263.55	0.66	1.13
425	2026.72	1.28	1137.80	5.54	0.92	0.56	1310.81	0.65	1.15
450	2145.93	1.32	1155.30	5.58	0.93	0.54	1356.69	0.63	1.17
475	2265.15	1.35	1167.95	5.53	0.94	0.52	1401.32	0.62	1.20
500	2384.37	1.39	1184.45	5.88	0.96	0.50	1444.79	0.61	1.22
700	3338.12	1.64	1299.45	14.82	1.05	0.39	1759.32	0.53	1.35
900	4291.87	1.86	1514.45	16.61	1.23	0.35	2031.28	0.47	1.34
1200	5722.49	2.15	1798.75	18.84	1.46	0.31	2387.59	0.42	1.33
1600	7629.99	2.48	2104.05	21.40	1.70	0.28	2799.02	0.37	1.33
2000	9537.49	2.78	2365.80	23.46	1.91	0.25	3161.49	0.33	1.34

## ANNEX B – DATA CONCERNING BEAMS AT ELEVATED TEMPERATURES

Tables B1 to B3 provide the numerical beam ultimate moments and their DSM estimates. Each table concerns one beam geometry (C120-C150-C160) and Pinned end support conditions, and provides information about the (i) steel yield stress  $\sigma_{y,20}$ , (ii) temperature value  $T$ , (iii) yield moment  $M_{y,T}$ , (iv) critical (distortional) buckling moment  $M_{cr,D,T}$ , (v) numerical ultimate moment  $M_{u,T}$  and associated  $(\delta/t)_{lim}$  value, (vi) DSM ultimate moment estimate  $M_{n,D,T}$ , (vii) distortional slenderness  $\bar{\lambda}_{D,T}$ , and (viii) ratios  $M_{u,T}/M_{y,T}$ ,  $M_{n,D,T}/M_{u,T}$  and  $M_{n,D,T}/M_{y,T}$ .

Table B1: Numerical ultimate loads and DSM estimates at elevated temperatures concerning the C120 beams analyzed.

$\sigma_{y,20}$ (MPa)	$T$ (°C)	$M_{y,T}$ (kN·cm)	$M_{cr,D,T}$ (kN·cm)	$\bar{\lambda}_{D,T}$	$M_{u,T}$ (kN·cm)	$(\delta/t)_{lim}$	$\frac{M_{u,T}}{M_{y,T}}$	$M_{n,D,T}$ (kN·cm)	$\frac{M_{n,D,T}}{M_{u,T}}$	$\frac{M_{n,D,T}}{M_{y,T}}$
250	20/100	930.99	1788.13	0.72	902.95	0.65	0.97	896.85	0.99	0.96
	200	828.58	1609.31	0.72	749.40	0.79	0.90	800.70	1.07	0.97
	300	726.17	1430.50	0.71	602.50	0.98	0.83	704.50	1.17	0.97
	400	605.14	1251.69	0.70	456.32	1.16	0.75	594.94	1.30	0.98
	500	493.42	1072.88	0.68	383.26	1.12	0.78	491.55	1.28	1.00
	600	279.30	554.32	0.71	202.16	1.24	0.72	271.52	1.34	0.97
	700	121.03	232.46	0.72	85.54	1.27	0.71	116.59	1.36	0.96
	800	65.17	160.93	0.64	52.44	0.86	0.80	65.17	1.24	1.00
500	20/100	1861.98	1788.13	1.02	1506.45	1.88	0.81	1431.29	0.95	0.77
	200	1657.16	1609.31	1.01	1286.60	1.59	0.78	1279.01	0.99	0.77
	300	1452.34	1430.50	1.01	1048.00	1.42	0.72	1126.67	1.08	0.78
	400	1210.28	1251.69	0.98	803.35	1.65	0.66	955.44	1.19	0.79
	500	986.85	1072.88	0.96	679.30	1.52	0.69	792.93	1.17	0.80
	600	558.59	554.32	1.00	354.85	1.77	0.64	434.50	1.22	0.78
	700	242.06	232.46	1.02	149.63	1.60	0.62	186.07	1.24	0.77
	800	130.34	160.93	0.90	94.65	1.32	0.73	109.42	1.16	0.84
700	20/100	2606.77	1788.13	1.21	1689.15	2.64	0.65	1765.60	1.05	0.68
	200	2320.02	1609.31	1.20	1485.30	2.44	0.64	1578.21	1.06	0.68
	300	2033.28	1430.50	1.19	1262.65	2.19	0.62	1390.75	1.10	0.68
	400	1694.40	1251.69	1.16	1000.60	1.94	0.59	1180.95	1.18	0.70
	500	1381.59	1072.88	1.13	851.00	1.95	0.62	981.45	1.15	0.71
	600	782.03	554.32	1.19	440.12	1.92	0.56	536.45	1.22	0.69
	700	338.88	232.46	1.21	185.17	2.04	0.55	229.53	1.24	0.68
	800	182.47	160.93	1.06	120.49	1.81	0.66	135.96	1.13	0.75
1200	20/100	4468.74	1788.13	1.58	1866.45	4.70	0.42	2433.39	1.30	0.54
	200	3977.18	1609.31	1.57	1661.15	4.50	0.42	2175.88	1.31	0.55
	300	3485.62	1430.50	1.56	1450.65	4.12	0.42	1918.27	1.32	0.55
	400	2904.68	1251.69	1.52	1222.80	3.57	0.42	1631.39	1.33	0.56
	500	2368.43	1072.88	1.49	1043.50	3.50	0.44	1358.03	1.30	0.57
	600	1340.62	554.32	1.56	540.80	3.59	0.40	740.10	1.37	0.55
	700	580.94	232.46	1.58	227.32	3.62	0.39	316.34	1.39	0.54
	800	312.81	160.93	1.39	152.85	3.01	0.49	188.96	1.24	0.60
1600	20/100	5958.32	1788.13	1.83	1960.45	5.78	0.33	2870.69	1.46	0.48
	200	5302.91	1609.31	1.82	1748.65	5.60	0.33	2567.26	1.47	0.48
	300	4647.49	1430.50	1.80	1534.25	5.38	0.33	2263.71	1.48	0.49
	400	3872.91	1251.69	1.76	1306.85	4.94	0.34	1926.37	1.47	0.50
	500	3157.91	1072.88	1.72	1113.50	4.68	0.35	1604.63	1.44	0.51
	600	1787.50	554.32	1.80	580.10	5.06	0.32	873.46	1.51	0.49
	700	774.58	232.46	1.83	244.23	5.18	0.32	373.19	1.53	0.48
	800	417.08	160.93	1.61	163.48	4.15	0.39	223.67	1.37	0.54
2000	20/100	7447.90	1788.13	2.04	2034.80	6.69	0.27	3255.97	1.60	0.44
	200	6628.63	1609.31	2.03	1818.75	6.50	0.27	2912.07	1.60	0.44
	300	5809.36	1430.50	2.02	1600.65	6.34	0.28	2568.05	1.60	0.44
	400	4841.14	1251.69	1.97	1371.75	5.99	0.28	2186.25	1.59	0.45
	500	3947.39	1072.88	1.92	1167.40	5.84	0.30	1821.89	1.56	0.46
	600	2234.37	554.32	2.01	610.05	6.16	0.27	990.95	1.62	0.44
	700	968.23	232.46	2.04	257.12	6.30	0.27	423.28	1.65	0.44
	800	521.35	160.93	1.80	171.36	5.27	0.33	254.25	1.48	0.49
2500	20/100	9309.88	1788.13	2.28	2105.40	7.70	0.23	3686.72	1.75	0.40
	200	8285.79	1609.31	2.27	1886.45	7.48	0.23	3297.59	1.75	0.40
	300	7261.71	1430.50	2.25	1665.60	7.26	0.23	2908.31	1.75	0.40
	400	6051.42	1251.69	2.20	1435.20	6.99	0.24	2476.81	1.73	0.41
	500	4934.24	1072.88	2.14	1220.80	6.78	0.25	2064.80	1.69	0.42
	600	2792.96	554.32	2.24	639.00	7.05	0.23	1122.31	1.76	0.40
	700	1210.28	232.46	2.28	269.36	7.37	0.22	479.27	1.78	0.40
	800	651.69	160.93	2.01	179.21	6.35	0.27	288.44	1.61	0.44

Table B2: Numerical ultimate loads and DSM estimates at elevated temperatures concerning the C150 beams analyzed.

$\sigma_{y,20}$ (MPa)	$T$ (°C)	$M_{v,T}$ (kN·cm)	$M_{cr,D,T}$ (kN·cm)	$\bar{\lambda}_{D,T}$	$M_{u,T}$ (kN·cm)	$(\delta/t)_{lim}$	$\frac{M_{u,T}}{M_{v,T}}$	$M_{n,D,T}$ (kN·cm)	$\frac{M_{n,D,T}}{M_{u,T}}$	$\frac{M_{n,D,T}}{M_{y,T}}$
250	20/100	1729.61	1904.00	0.95	1633.80	1.41	0.94	1395.83	0.85	0.81
	200	1539.36	1713.60	0.95	1398.80	1.30	0.91	1247.15	0.89	0.81
	300	1349.10	1523.20	0.94	1132.45	0.97	0.84	1098.40	0.97	0.81
	400	1124.25	1332.80	0.92	835.60	1.04	0.74	930.88	1.11	0.83
	500	916.70	1142.40	0.90	711.60	0.97	0.78	772.02	1.08	0.84
	600	518.88	590.24	0.94	364.66	1.17	0.70	423.56	1.16	0.82
	700	224.85	247.52	0.95	152.99	1.20	0.68	181.46	1.19	0.81
	800	121.07	171.36	0.84	99.37	1.02	0.82	106.34	1.07	0.88
500	20/100	3459.23	1904.00	1.35	1916.85	3.07	0.55	2147.51	1.12	0.62
	200	3078.71	1713.60	1.34	1701.00	2.83	0.55	1919.89	1.13	0.62
	300	2698.20	1523.20	1.33	1476.90	2.53	0.55	1692.18	1.15	0.63
	400	2248.50	1332.80	1.30	1228.50	1.97	0.55	1437.91	1.17	0.64
	500	1833.39	1142.40	1.27	1051.15	1.95	0.57	1195.90	1.14	0.65
	600	1037.77	590.24	1.33	540.30	1.96	0.52	652.79	1.21	0.63
	700	449.70	247.52	1.35	226.47	1.95	0.50	279.18	1.23	0.62
	800	242.15	171.36	1.19	153.63	1.82	0.63	166.00	1.08	0.69
700	20/100	4842.92	1904.00	1.59	2042.55	4.94	0.42	2617.72	1.28	0.54
	200	4310.20	1713.60	1.59	1812.10	4.66	0.42	2340.72	1.29	0.54
	300	3777.48	1523.20	1.57	1576.45	3.99	0.42	2063.62	1.31	0.55
	400	3147.90	1332.80	1.54	1328.20	3.00	0.42	1755.08	1.32	0.56
	500	2566.75	1142.40	1.50	1135.35	2.94	0.44	1461.05	1.29	0.57
	600	1452.88	590.24	1.57	586.70	2.97	0.40	796.18	1.36	0.55
	700	629.58	247.52	1.59	246.35	3.15	0.39	340.30	1.38	0.54
	800	339.00	171.36	1.41	167.13	2.51	0.49	203.32	1.22	0.60
1200	20/100	8302.15	1904.00	2.09	2326.45	7.93	0.28	3556.96	1.53	0.43
	200	7388.91	1713.60	2.08	2068.90	7.58	0.28	3181.33	1.54	0.43
	300	6475.68	1523.20	2.06	1805.75	7.19	0.28	2805.56	1.55	0.43
	400	5396.40	1332.80	2.01	1523.05	6.39	0.28	2388.63	1.57	0.44
	500	4400.14	1142.40	1.96	1295.15	6.24	0.29	1990.71	1.54	0.45
	600	2490.64	590.24	2.05	676.35	6.44	0.27	1082.62	1.60	0.43
	700	1079.28	247.52	2.09	285.05	6.69	0.26	462.40	1.62	0.43
	800	581.15	171.36	1.84	188.84	5.63	0.32	277.87	1.47	0.48
1600	20/100	11069.53	1904.00	2.41	2495.30	9.22	0.23	4172.02	1.67	0.38
	200	9851.88	1713.60	2.40	2226.10	9.06	0.23	3731.80	1.68	0.38
	300	8634.24	1523.20	2.38	1951.80	8.74	0.23	3291.42	1.69	0.38
	400	7195.20	1332.80	2.32	1657.35	8.12	0.23	2803.52	1.69	0.39
	500	5866.85	1142.40	2.27	1407.05	7.94	0.24	2337.55	1.66	0.40
	600	3320.86	590.24	2.37	737.75	8.21	0.22	1270.18	1.72	0.38
	700	1439.04	247.52	2.41	311.29	8.45	0.22	542.36	1.74	0.38
	800	774.87	171.36	2.13	204.59	7.28	0.26	326.69	1.60	0.42
2000	20/100	13836.92	1904.00	2.70	2556.45	8.40	0.18	4713.91	1.84	0.34
	200	12314.85	1713.60	2.68	2294.55	8.41	0.19	4216.78	1.84	0.34
	300	10792.79	1523.20	2.66	2057.60	9.62	0.19	3719.47	1.81	0.34
	400	8994.00	1332.80	2.60	1762.05	9.19	0.20	3169.04	1.80	0.35
	500	7333.57	1142.40	2.53	1495.95	9.02	0.20	2643.13	1.77	0.36
	600	4151.07	590.24	2.65	785.10	9.22	0.19	1435.44	1.83	0.35
	700	1798.80	247.52	2.70	331.22	9.44	0.18	612.81	1.85	0.34
	800	968.58	171.36	2.38	217.82	8.53	0.22	369.70	1.70	0.38
2500	20/100	17296.14	1904.00	3.01	2646.95	9.57	0.15	5319.75	2.01	0.31
	200	15393.57	1713.60	3.00	2374.80	9.41	0.15	4759.00	2.00	0.31
	300	13490.99	1523.20	2.98	2065.30	8.29	0.15	4198.05	2.03	0.31
	400	11242.49	1332.80	2.90	1830.70	9.12	0.16	3577.70	1.95	0.32
	500	9166.96	1142.40	2.83	1568.50	9.23	0.17	2984.77	1.90	0.33
	600	5188.84	590.24	2.96	811.65	9.10	0.16	1620.19	2.00	0.31
	700	2248.50	247.52	3.01	340.88	9.20	0.15	691.57	2.03	0.31
	800	1210.73	171.36	2.66	228.59	8.69	0.19	417.79	1.83	0.35

Table B3: Numerical ultimate loads and DSM estimates at elevated temperatures concerning the C160 beams analyzed.

$\sigma_{y,20}$ (MPa)	$T$ (°C)	$M_{y,T}$ (kN·cm)	$M_{cr,D,T}$ (kN·cm)	$\bar{\lambda}_{D,T}$	$M_{u,T}$ (kN·cm)	$(\delta/l)_{lim}$	$\frac{M_{u,T}}{M_{y,T}}$	$M_{n,D,T}$ (kN·cm)	$\frac{M_{n,D,T}}{M_{u,T}}$	$\frac{M_{n,D,T}}{M_{y,T}}$
250	20/100	1192.19	841.82	1.19	805.79	2.65	0.68	816.60	1.01	0.68
	200	1061.05	757.64	1.18	711.46	2.45	0.67	729.92	1.03	0.69
	300	929.91	673.46	1.18	603.83	2.09	0.65	643.20	1.07	0.69
	400	774.92	589.27	1.15	460.27	1.37	0.59	546.11	1.19	0.70
	500	631.86	505.09	1.12	393.71	1.32	0.62	453.81	1.15	0.72
	600	357.66	260.96	1.17	199.88	1.50	0.56	248.10	1.24	0.69
	700	154.98	109.44	1.19	83.58	1.58	0.54	106.16	1.27	0.68
	800	83.45	75.76	1.05	55.69	1.23	0.67	62.85	1.13	0.75
500	20/100	2384.37	841.82	1.68	893.30	5.21	0.37	1231.56	1.38	0.52
	200	2122.09	757.64	1.67	793.65	4.94	0.37	1101.30	1.39	0.52
	300	1859.81	673.46	1.66	692.80	4.54	0.37	970.99	1.40	0.52
	400	1549.84	589.27	1.62	588.25	3.83	0.38	826.02	1.40	0.53
	500	1263.72	505.09	1.58	503.20	3.81	0.40	687.81	1.37	0.54
	600	715.31	260.96	1.66	259.90	3.79	0.36	374.64	1.44	0.52
	700	309.97	109.44	1.68	109.05	3.94	0.35	160.10	1.47	0.52
	800	166.91	75.76	1.48	74.33	3.72	0.45	95.78	1.29	0.57
700	20/100	3338.12	841.82	1.99	946.60	7.00	0.28	1491.13	1.58	0.45
	200	2970.93	757.64	1.98	841.80	6.78	0.28	1333.62	1.58	0.45
	300	2603.73	673.46	1.97	734.95	6.51	0.28	1176.04	1.60	0.45
	400	2169.78	589.27	1.92	624.00	5.47	0.29	1001.11	1.60	0.46
	500	1769.20	505.09	1.87	532.10	5.66	0.30	834.19	1.57	0.47
	600	1001.44	260.96	1.96	275.35	5.08	0.27	453.80	1.65	0.45
	700	433.96	109.44	1.99	115.80	5.31	0.27	193.85	1.67	0.45
	800	233.67	75.76	1.76	77.98	4.16	0.33	116.39	1.49	0.50
1200	20/100	8302.15	841.82	3.14	1051.60	9.59	0.13	2458.46	2.34	0.30
	200	7388.91	757.64	3.12	936.40	9.51	0.13	2199.35	2.35	0.30
	300	6475.68	673.46	3.10	821.00	9.64	0.13	1940.16	2.36	0.30
	400	5396.40	589.27	3.03	700.95	9.39	0.13	1653.60	2.36	0.31
	500	4400.14	505.09	2.95	596.45	9.16	0.14	1379.68	2.31	0.31
	600	2490.64	260.96	3.09	311.53	9.39	0.13	748.79	2.40	0.30
	700	1079.28	109.44	3.14	131.24	9.55	0.12	319.60	2.44	0.30
	800	581.15	75.76	2.77	87.40	8.31	0.15	193.17	2.21	0.33
1600	20/100	7629.99	841.82	3.01	1105.80	11.70	0.14	2349.18	2.12	0.31
	200	6790.69	757.64	2.99	987.65	11.41	0.15	2101.55	2.13	0.31
	300	5951.39	673.46	2.97	868.85	11.39	0.15	1853.84	2.13	0.31
	400	4959.49	589.27	2.90	745.30	11.10	0.15	1579.89	2.12	0.32
	500	4043.89	505.09	2.83	634.15	10.88	0.16	1318.05	2.08	0.33
	600	2289.00	260.96	2.96	331.53	11.33	0.14	715.47	2.16	0.31
	700	991.90	109.44	3.01	139.68	11.52	0.14	305.39	2.19	0.31
	800	534.10	75.76	2.66	92.96	10.28	0.17	184.49	1.98	0.35
2000	20/100	9537.49	841.82	3.37	1142.90	13.95	0.12	2648.32	2.32	0.28
	200	8488.36	757.64	3.35	1023.25	13.65	0.12	2369.28	2.32	0.28
	300	7439.24	673.46	3.32	902.65	13.27	0.12	2090.14	2.32	0.28
	400	6199.37	589.27	3.24	777.45	12.74	0.13	1781.67	2.29	0.29
	500	5054.87	505.09	3.16	661.85	12.31	0.13	1486.75	2.25	0.29
	600	2861.25	260.96	3.31	345.83	13.03	0.12	806.70	2.33	0.28
	700	1239.87	109.44	3.37	145.65	13.39	0.12	344.28	2.36	0.28
	800	667.62	75.76	2.97	97.21	11.68	0.15	208.24	2.14	0.31
2500	20/100	11921.86	841.82	3.76	1172.00	16.22	0.10	2982.77	2.55	0.25
	200	10610.45	757.64	3.74	1052.35	15.93	0.10	2668.61	2.54	0.25
	300	9299.05	673.46	3.72	931.35	15.38	0.10	2354.34	2.53	0.25
	400	7749.21	589.27	3.63	805.75	14.58	0.10	2007.28	2.49	0.26
	500	6318.59	505.09	3.54	686.60	14.19	0.11	1675.35	2.44	0.27
	600	3576.56	260.96	3.70	358.26	14.97	0.10	908.69	2.54	0.25
	700	1549.84	109.44	3.76	150.78	15.07	0.10	387.76	2.57	0.25
	800	834.53	75.76	3.32	101.13	12.98	0.12	234.78	2.32	0.28